

1 **Bone marrow adipose tissue is a unique adipose subtype with distinct roles in**  
2 **systemic glucose homeostasis**

3  
4 **Running Title:** Marrow adipose tissue is a distinct, major subtype of adipose tissue

5  
6 Karla J. Suchacki<sup>1</sup>, Adriana A.S. Tavares<sup>1</sup>, Domenico Mattiucci<sup>1,2</sup>, Erica L. Scheller<sup>3</sup>,  
7 Giorgos Papanastasiou<sup>4</sup>, Calum Gray<sup>4</sup>, Matthew C. Sinton<sup>1</sup>, Lynne E. Ramage<sup>1</sup>, Wendy A.  
8 McDougald<sup>1</sup>, Andrea Lovdel<sup>1</sup>, Richard J. Sulston<sup>1</sup>, Benjamin J. Thomas<sup>1</sup>, Bonnie M.  
9 Nicholson<sup>1</sup>, Amanda J. Drake<sup>1</sup>, Carlos J. Alcaide-Corral<sup>1</sup>, Diana Said<sup>1</sup>, Antonella Poloni<sup>2</sup>,  
10 Saverio Cinti<sup>2,5</sup>, Gavin J. MacPherson<sup>6</sup>, Marc R. Dweck<sup>1</sup>, Jack P.M. Andrews<sup>1</sup>, Michelle C.  
11 Williams<sup>1</sup>, Robert J. Wallace<sup>7</sup>, Edwin J.R. van Beek<sup>4</sup>, Ormond A. MacDougald<sup>8</sup>, Nicholas M.  
12 Morton<sup>1</sup>, Roland H. Stimson<sup>1</sup> and William P. Cawthorn<sup>1\*</sup>.

13  
14 <sup>1</sup>University/BHF Centre for Cardiovascular Science, University of Edinburgh, The Queen's  
15 Medical Research Institute, Edinburgh BioQuarter, 47 Little France Crescent, Edinburgh,  
16 EH16 4TJ, Scotland, UK. <sup>2</sup>Dipartimento di Scienze Cliniche e Molecolari, Clinica di  
17 Ematologia, Università Politecnica delle Marche, Ancona, Italy. <sup>3</sup>Division of Bone and  
18 Mineral Diseases, Department of Medicine, Washington University, St. Louis, MO, USA.  
19 <sup>4</sup>Edinburgh Imaging, University of Edinburgh, UK. <sup>5</sup>Dipartimento di Medicina Sperimentale  
20 e Clinica, Center of Obesity, Università Politecnica delle Marche, Ancona, Italy. <sup>6</sup>Department  
21 of Orthopaedic Surgery, Royal Infirmary Edinburgh, UK. <sup>7</sup>Department of Orthopaedics, The  
22 University of Edinburgh, UK. <sup>8</sup>Department of Molecular & Integrative Physiology, University  
23 of Michigan, Ann Arbor, MI, USA.

24  
25  
26 **\*Correspondence to:** William Cawthorn, University/BHF Centre for Cardiovascular  
27 Science, The Queen's Medical Research Institute, Edinburgh BioQuarter, 47 Little France  
28 Crescent, Edinburgh, EH16 4TJ. [W.Cawthorn@ed.ac.uk](mailto:W.Cawthorn@ed.ac.uk)

29  
30  
31  
32 **Keywords:**

33 Bone marrow adipose tissue, bone marrow adipocytes, white adipose tissue, brown adipose  
34 tissue, beige adipose tissue, PET/CT, glucose homeostasis, insulin, cold exposure, bone

35 **HIGHLIGHTS**

36

37 • Bone marrow adipose tissue (BMAT) is molecularly distinct to other adipose  
38 subtypes.

39 • BMAT is less insulin responsive than WAT and, unlike BAT, is not cold-responsive.

40 • Human BMAT has greater basal glucose uptake than axial bone or subcutaneous  
41 WAT.

42 • We establish a PET/CT method for BMAT localisation and functional analysis *in vivo*.

43 **SUMMARY**

44

45 Bone marrow adipose tissue (BMAT) represents >10% of total adipose mass, yet unlike  
46 white or brown adipose tissues (WAT or BAT), its role in systemic metabolism remains  
47 unclear. Using transcriptomics, we reveal that BMAT is molecularly distinct to WAT but is  
48 not enriched for brown or beige adipocyte markers. Instead, pathway analysis indicated  
49 altered glucose metabolism and decreased insulin responsiveness in BMAT. We therefore  
50 tested these functions in mice and humans using positron emission tomography–computed  
51 tomography (PET/CT) with <sup>18</sup>F-fluorodeoxyglucose, including establishing a new method for  
52 BMAT identification from clinical CT scans. This revealed that BMAT resists insulin- and  
53 cold-stimulated glucose uptake and is thus functionally distinct to WAT and BAT. However,  
54 BMAT displayed greater basal glucose uptake than axial bones or subcutaneous WAT,  
55 underscoring its potential to influence systemic glucose homeostasis. These PET/CT  
56 studies are the first to characterise BMAT function *in vivo* and identify BMAT as a distinct,  
57 major subtype of adipose tissue.

## 58 INTRODUCTION

59

60 Adipose tissue plays a fundamental role in systemic energy homeostasis. In mammals it is  
61 typically classified into two major subtypes: white adipose tissue (WAT), which stores and  
62 releases energy and has diverse endocrine functions; and brown adipose tissue (BAT),  
63 which mediates adaptive thermogenesis (Cinti, 2018). Cold exposure and other stimuli also  
64 cause the emergence of brown-like adipocytes within WAT, typically referred to as “beige”  
65 adipocytes (Cinti, 2018). White, brown and beige adipocytes have attracted extensive  
66 research interest, owing largely to their roles and potential as therapeutic targets in  
67 metabolic diseases.

68

69 Adipocytes are also a major cell type within the bone marrow (BM), accounting for up to  
70 70% of BM volume. Indeed, this BM adipose tissue (BMAT) can represent over 10% of total  
71 adipose tissue mass in healthy adults (Cawthorn et al., 2014). BMAT further accumulates in  
72 diverse physiological and clinical conditions, including aging, obesity, type 2 diabetes and  
73 osteoporosis, as well as therapeutic contexts such as radiotherapy or glucocorticoid  
74 treatment. Strikingly, BMAT also increases in states of caloric restriction (Scheller et al.,  
75 2016). These observations suggest that BMAT is distinct to WAT and BAT and might impact  
76 the pathogenesis of diverse diseases. However, unlike WAT and BAT, the role of BMAT in  
77 systemic energy homeostasis remains poorly understood.

78

79 The metabolic importance of WAT is highlighted in situations of both WAT excess (obesity)  
80 and deficiency (lipodystrophy), each of which leads to systemic metabolic dysfunction (Cinti,  
81 2018). This largely reflects the key role of WAT as an insulin target tissue. Adipocyte-specific  
82 ablation of the insulin receptor in mice causes insulin resistance, glucose intolerance and  
83 dyslipidaemia (Qiang et al., 2016; Sakaguchi et al., 2017). Similar effects result from  
84 adipocytic deletion of *Slc2a4* (Glut4), the insulin-sensitive glucose transporter (Abel et al.,  
85 2001). Conversely, adipocyte-specific overexpression of *Slc2a4* reverses insulin resistance  
86 and diabetes in mice predisposed to diabetes (Carvalho et al., 2005). Thus, insulin-  
87 stimulated glucose uptake is fundamental to WAT’s role in systemic metabolic homeostasis.

88

89 In contrast to WAT, the defining function of BAT is in mediating adaptive thermogenesis via  
90 uncoupled respiration. This is driven by mitochondria expressing uncoupling protein-1  
91 (UCP1), which are abundant in brown adipocytes. Cold exposure is the classical stimulator  
92 of BAT activity: cold-induced glucose uptake is a hallmark of BAT activation and can be  
93 quantified *in vivo* using positron emission tomography–computed tomography (PET/CT)  
94 with <sup>18</sup>F-fluorodeoxyglucose (<sup>18</sup>F-FDG) (Cinti, 2018; Ramage et al., 2016a). Cold exposure  
95 or chronic sympathetic stimulation exert similar effects on beige adipocytes, and activation  
96 of brown or beige adipocytes can enhance energy expenditure (Cinti, 2018). Consequently,  
97 the past decade has seen extensive interest in activating BAT, or promoting beiging of WAT,  
98 to treat metabolic disease (Cinti, 2018).

99

100 Compared to WAT and BAT, study of BMAT has been relatively limited. However, given its  
101 abundance and clinical potential (Scheller et al., 2016), BMAT is now attracting increasing  
102 attention, with several studies beginning to investigate its metabolic properties. BM  
103 adipocytes (BMAds) have been proposed to exist in two broad subtypes: ‘constitutive’  
104 BMAds (cBMAds) appear as contiguous groups of adipocytes that predominate at distal  
105 skeletal sites, whereas ‘regulated’ BMAds (rBMAds) occur interspersed with the  
106 haematopoietic BM in the proximal and axial skeleton (Craft et al., 2018). Both subtypes are  
107 morphologically similar to white adipocytes, with large unilocular lipid droplets; however,  
108 their lipid content differs, with cBMAds having a greater proportion of unsaturated fatty acids  
109 than rBMAds or white adipocytes (Scheller et al., 2016). Like white adipocytes, BMAds also

110 produce adipokines such as leptin and adiponectin (Sulston and Cawthorn, 2016) and can  
111 release free fatty acids in response to lipolytic stimuli, albeit to a lesser extent than WAT  
112 (Scheller et al., 2018; Tran et al., 1981). This lipolysis resistance is more pronounced for  
113 rBMAds, underscoring the functional differences in BMAd subtypes.

114  
115 Despite these advances in understanding of BMAT lipid metabolism, its insulin  
116 responsiveness and role in systemic glucose homeostasis is poorly understood. PET/CT  
117 studies have demonstrated glucose uptake into whole bones or BM of animal models and  
118 humans (Huovinen et al., 2016; Huovinen et al., 2014; Nishio et al., 2012; Zoch et al., 2016),  
119 but uptake specifically into BMAT has not previously been examined. Whether BMAT is  
120 BAT- or beige-like is also debated (Scheller et al., 2016). UCP-1 positive adipocytes have  
121 been noted in vertebral BM of a young mouse (Nishio et al., 2012) and as an incidental  
122 finding in one clinical case study (Chapman and Vega, 2017), but most studies find very low  
123 skeletal UCP-1 expression (Krings et al., 2012; Sulston et al., 2016). It has been suggested  
124 that BMAT is BAT-like, albeit based only on transcript expression from whole bones (Krings  
125 et al., 2012). Notably, no studies have fully investigated if BMAT has properties of BAT or  
126 beige fat *in vivo*. Together, it remains unclear if BMAT performs metabolic functions similar  
127 to WAT, BAT or beige adipose tissue.

128  
129 Herein, we used transcriptomic analysis and <sup>18</sup>F-FDG PET/CT to address these  
130 fundamental gaps in knowledge and thereby determine if, *in vivo*, BMAT has metabolic  
131 functions of WAT or BAT. Our studies in animal models and humans demonstrate that BMAT  
132 is transcriptionally and functionally distinct to WAT, BAT and beige adipose tissue,  
133 identifying BMAT as a unique class of adipose tissue. We show that BMAT has greater basal  
134 glucose uptake than WAT and establish methods for BMAT characterisation by PET/CT.  
135 Together, this knowledge underscores the potential for BMAT to influence metabolic  
136 homeostasis and sets a foundation for future research to reveal further roles of BMAT in  
137 normal physiology and disease.

## 138 RESULTS

139

### 140 **BMAT is transcriptionally distinct to WAT, BAT and beige adipose tissues**

141 The functional hallmarks of WAT, BAT and beige adipose tissue are reflected on a molecular  
142 level, with each class having distinct transcriptomic profiles and characteristic marker genes  
143 (Rosell et al., 2014; Svensson et al., 2011; Wu et al., 2012). Thus, to test if BMAT has distinct  
144 metabolic functions, we first compared the transcriptomes of whole BMAT and WAT from  
145 two cohorts of rabbits. Principle component analysis of both cohorts identified BMAT as a  
146 distinct depot compared to gonadal WAT (gWAT) and inguinal WAT (iWAT) (Fig. 1A);  
147 however, BMAT from either rabbit cohort was not uniformly enriched for markers of brown  
148 or beige adipocytes (Fig. 1B, S1A): although *SLC27A2* was significantly higher in BMAT  
149 than WAT from both cohorts, and *PPARGC1A* in BMAT from cohort 1, several other brown  
150 and/or beige markers were more highly expressed in WAT, while most such markers were  
151 not differentially expressed between BMAT and WAT in either cohort (Fig. 1B, S1A). Thus,  
152 the transcriptomic distinction with WAT is not a result of BMAT being more brown- or beige-  
153 like. Instead, gene set enrichment analysis (GSEA) highlighted the potential for BMAT to  
154 have altered glucose metabolism and decreased insulin responsiveness compared to WAT  
155 (Fig. 1C,1D, S1B).

156

157 To determine if similar differences occur in humans, we next analysed the transcriptomes of  
158 adipocytes isolated from human femoral BMAT and subcutaneous WAT, which our previous  
159 analyses revealed to be globally distinct (Mattiucci et al., 2018). Consistent with our findings  
160 in rabbits, human BMAd were not enriched for brown or beige markers and had decreased  
161 expression of genes relating to glucose metabolism and insulin responsiveness (Fig. 1E,  
162 S2A, S2B). To further address this we next pursued targeted analysis of adipocytes isolated  
163 from BM and WAT of a second cohort of subjects; we also isolated adipocytes from  
164 trabecular bone (Bone Ads) to assess potential site-specific differences in BMAd function  
165 (Craft et al., 2018). Adipocyte purity was confirmed histologically (data not shown) and by  
166 qPCR (Fig. S2C). *In situ*, these BM and bone adipocytes resembled unilocular white  
167 adipocytes (Fig. 1F); however, qPCR revealed significant differences in transcript  
168 expression of *INSR*, *IRS1*, *IRS2*, *SLC2A4*, *SLC2A1* and *SLC2A3* between WAT adipocytes  
169 and those from BM or bone (Fig. 1G). Notably, compared to white adipocytes, each BMAd  
170 subtype had decreased *SLC2A4* and increased *SLC2A1* and *SLC2A3*, suggesting that  
171 BMAds may have higher basal glucose uptake that is less insulin responsive. In contrast,  
172 there were no differences in expression of *UCP1*, and most other brown or beige adipocyte  
173 markers were not enriched in either BMAd subtype (Fig. 1G, S2D).

174

175 Taken together, these data demonstrate that BMAds in animal models and humans are  
176 transcriptionally distinct to white, brown and beige adipocytes, and suggest altered roles in  
177 systemic glucose homeostasis and insulin responsiveness.

178

### 179 **Insulin treatment in mice does not induce glucose uptake in BMAT**

180 To test the metabolic functions of BMAT *in vivo* we used <sup>18</sup>F-FDG PET/CT in mice to  
181 determine if, like WAT, BMAT is insulin-responsive. As expected, insulin decreased blood  
182 glucose (Fig. 2A) and increased <sup>18</sup>F-FDG uptake in the heart, iWAT and gWAT (Fig. 2B, C  
183 and F). To assess <sup>18</sup>F-FDG uptake separately within bone and BMAT, we first applied  
184 thresholding to the PET/CT data to separate bone from BM based on their different tissue  
185 densities (*data not shown*). This revealed that insulin significantly increased <sup>18</sup>F-FDG uptake  
186 in femoral bone, whereas humoral bone uptake decreased; uptake in proximal or distal tibial  
187 bone was unaffected (Fig. 2F). To assess BMAT-specific <sup>18</sup>F-FDG uptake we took  
188 advantage of the regional differences in BMAT content around the mouse skeleton. Thus,  
189 adipocytes comprise only a small percentage of total BM volume of humeri, femurs and

190 proximal tibiae, but predominate in distal tibiae (Fig. 2E). To address the contribution of  
191 BMAT to skeletal  $^{18}\text{F}$ -FDG uptake, we therefore quantified  $^{18}\text{F}$ -FDG in a bone-region-specific  
192 manner to distinguish between areas of low BMAT (humerus, femur, proximal tibia) and high  
193 BMAT (distal tibia). This revealed that insulin did not significantly affect glucose uptake in  
194 any of the BM regions analysed (Fig. 2F). Thus, compared to WAT, BM and BMAT resist  
195 insulin-stimulated glucose uptake.

196

### 197 ***Cold exposure in mice does not induce glucose uptake or beiging in BMAT***

198 To test if BMAT is BAT- or beige-like *in vivo*, we next analysed  $^{18}\text{F}$ -FDG uptake following  
199 acute or chronic cold exposure in mice (Fig. S3A). Acute (4 h) or chronic cold (72 h)  
200 increased energy expenditure without causing weight loss or hypoglycaemia (Fig. S3B-D),  
201 likely due to increased food consumption in chronic cold mice (Fig. S3E). BAT  $^{18}\text{F}$ -FDG  
202 uptake increased after either duration of cold (Fig. 3A-C). Chronic cold also increased iWAT  
203  $^{18}\text{F}$ -FDG uptake, suggesting beiging of this depot (Fig. 3C). However, neither acute nor  
204 chronic cold exposure increased  $^{18}\text{F}$ -FDG uptake into bone or BM (Fig. 3B). Indeed, cold  
205 exposure decreased  $^{18}\text{F}$ -FDG uptake into distal tibial BMAT, highlighting fundamental  
206 differences with iWAT and BAT. Cold exposure also decreased BAT lipid content and  
207 promoted beiging of iWAT, as indicated by formation of multilocular adipocytes, but these  
208 effects did not occur in BMAT (Fig. 3D). Consistent with this, cold exposure induced brown  
209 and beige transcripts in BAT and iWAT, but not within bone (Fig. 3E-G, S3F-H). Housing  
210 control mice at room temperature (22 °C) might have caused a mild cold stress, preventing  
211 detection of further beiging at 4 °C; however, even when compared to mice at  
212 thermoneutrality (28 °C), cold exposure did not induce a beiging response within bones (Fig.  
213 S3I). These results show that, *in vivo*, BMAT is functionally distinct to brown and beige  
214 adipose tissues.

215

### 216 ***CT-based identification of BMAT in humans***

217 We next tested if these distinct metabolic properties extend to BMAT in humans. First, we  
218 established a method to identify BMAT from clinical PET/CT scans. To determine Hounsfield  
219 Units (HU) for BMAT, we identified BMAT-rich and BMAT-deficient BM regions by magnetic  
220 resonance imaging (MRI). This revealed that sternal BM is BMAT-enriched while vertebral  
221 BM is BMAT-deficient (Fig. 4A); WAT was also analysed as an adipose-rich control region.  
222 We then co-registered the MRI data with paired CT scans of the same subjects (Fig. 4A).  
223 This revealed a distinct HU distribution for BMAT-rich sternal BM, intermediate between  
224 WAT and red marrow (RM) of BMAT-deficient vertebrae (Fig. 4B).

225

226 Using these distinct HU distributions, we generated a receiver operating characteristic  
227 (ROC) curve to identify optimal diagnostic HU thresholds to distinguish BMAT from RM (Fig.  
228 S4A). This revealed that BMAT-rich BM has HU <115, whereas RM is mostly within 115-  
229 300 HU (Fig. 4B); bone was defined as >300 HU. To test the validity of these thresholds we  
230 applied them to clinical CT data to determine BMAT volume as % BM volume. We found  
231 that BMAT predominated in the arms, legs and sternum but was markedly lower in the  
232 clavicle, ribs and vertebrae (Fig. 4C, Fig. S4B). Moreover, %BMAT showed age-associated  
233 increases in the axial skeleton but not in long bones (Fig. S4B). These data are consistent  
234 with previous studies showing that BMAT predominates in the long bones by early adulthood  
235 but continues to accumulate in axial bones beyond 60 years of age (Baum et al., 2018;  
236 Kricun, 1985; Schraml et al., 2015). Together, this supports the validity of our CT thresholds  
237 for BMAT identification in humans.

238

239

240

241 ***Human BMAT is functionally distinct to BAT and is a major site of basal glucose***  
242 ***uptake***

243 We then applied these thresholds to human co-registered PET/CT data to assess  $^{18}\text{F}$ -FDG  
244 uptake in BMAT, RM and bone. To test if BMAT is BAT-like we first compared BMAT  $^{18}\text{F}$ -  
245 FDG uptake between three groups: subjects with no detectable supraclavicular BAT at room  
246 temperature (*No BAT*), subjects with active BAT at room temperature (*Active BAT*), and  
247 cold-exposed subjects (16 °C for 2 h; *Cold*). PET/CT confirmed BAT  $^{18}\text{F}$ -FDG uptake in the  
248 latter two groups but not in the *No BAT* group (Fig. 4D-E, Fig. S4C). Cold exposure did not  
249 alter  $^{18}\text{F}$ -FDG uptake in scWAT but was associated with increased uptake in sternal and  
250 clavicular bone tissue; however, these were the only skeletal sites at which  $^{18}\text{F}$ -FDG uptake  
251 significantly differed between the *No BAT*, *Active BAT* and *Cold* subjects (Fig. 4E, Fig. S4D).  
252 Indeed, the *Active BAT* and *Cold* subjects did not have increased glucose uptake in BMAT  
253 or RM of any bones analysed (Fig. 4E, Fig. S4D). Thus, consistent with our findings in mice,  
254 BMAT glucose uptake in humans is not cold-responsive.  
255

256 Our previous human PET/CT studies revealed that glucocorticoids acutely activate BAT  
257 (Ramage et al., 2016a). Glucocorticoids also promote BMAT accumulation, demonstrating  
258 that BMAT can be glucocorticoid-responsive (Scheller et al., 2016). Thus, to further test if  
259 BMAT shares properties of BAT, we analysed PET/CT data from previously reported  
260 subjects (Ramage et al., 2016a) to determine if glucocorticoids also influence glucose  
261 uptake in human BMAT. We found that prednisolone significantly influenced  $^{18}\text{F}$ -FDG uptake  
262 only in vertebrae, in which there was a trend for increased uptake into RM but not BMAT or  
263 bone (Fig. S4E). However, prednisolone did not influence  $^{18}\text{F}$ -FDG uptake at any other site.  
264 Thus, unlike BAT, BMAT glucose uptake is not glucocorticoid-responsive.  
265

266 The above findings confirm that, in humans, BMAT is functionally distinct to BAT. However,  
267 while analyzing these data, two other phenomena became apparent. Firstly, within axial  
268 bones of each subject, BMAT had significantly higher glucose uptake than bone (Fig. 4F).  
269 In the sternum, glucose uptake was also greater in BMAT than in RM (Fig. 4F). Secondly,  
270 BMAT at each skeletal site had higher glucose uptake than scWAT (Fig. 4G). Thus, despite  
271 being unresponsive to insulin or activators of BAT, BMAT has high basal glucose uptake,  
272 highlighting its potential to influence systemic glucose homeostasis.



## 273 DISCUSSION

274

275 Unlike WAT and BAT, the role of BMAT in systemic energy metabolism is poorly understood.  
276 Previous studies have shed some light on BMAT lipid metabolism *in vivo* (Scheller et al.,  
277 2018; Tran et al., 1981), and PET/CT has been used to assess glucose uptake into bones  
278 or BM (Huovinen et al., 2016; Huovinen et al., 2014; Nishio et al., 2012; Zoch et al., 2016);  
279 however, our study is the first to characterise *in vivo* glucose metabolism specifically in  
280 BMAT. Our data provide key insights into how BMAT compares to WAT and BAT; reveal  
281 new site-specific differences in BMAT characteristics; and identify BMAT as a major site of  
282 skeletal glucose disposal. Moreover, we establish a method for BMAT identification and  
283 analysis by PET/CT that will open new avenues for future study of BMAT function.

284

285 We show, for the first time, that, compared to WAT, BMAT resists insulin-stimulated glucose  
286 uptake. This is supported not only by PET/CT of mouse distal tibial BMAT, but also by the  
287 transcriptional profiles of rabbit and human BMAT from other skeletal sites. This conclusion  
288 seemingly contrasts with findings elsewhere. For example, adipocyte-specific ablation of  
289 *Insr* in mice decreases BMAd size (Qiang et al., 2016), suggesting a role for insulin in BMAd  
290 lipogenesis; however, it is unclear if this is through *de novo* lipogenesis from glucose, or via  
291 insulin regulating uptake and esterification of fatty acids. In humans, Huovinen *et al* used  
292 PET/CT to assess BM <sup>18</sup>F-FDG uptake during hyperinsulinaemic euglycemic clamp,  
293 concluding that whole BM may be insulin-responsive (Huovinen et al., 2016). Thus, one  
294 possibility is that insulin can stimulate BMAT glucose uptake under hyperinsulinaemic  
295 conditions. However, unlike our work, Huovinen *et al* did not distinguish BMAT-rich from  
296 BMAT-deficient BM, nor did they use a vehicle control to confirm if BM <sup>18</sup>F-FDG uptake is  
297 genuinely insulin-responsive. Indeed, microarrays show that *SLC2A4* and *IRS1* expression  
298 is negligible in human BM (Dezso et al., 2008), while *Slc2a4* and *Irs1* are markedly lower in  
299 BM than in WAT or muscle of mice (Thorrez et al., 2008). More recent microarrays show  
300 that *Slc2a4*, *Insr*, *Irs1* and *Irs2* are lower in BMAds than epididymal white adipocytes of mice  
301 (Liu et al., 2011). These data are strikingly consistent with our results for transcript  
302 expression in rabbits and humans (Fig. 1, Fig. S1-2) and further support the conclusion that,  
303 compared to WAT, BMAT resists insulin-stimulated glucose uptake.

304

305 In addition to BMAT, we also found that insulin responsiveness varies among different  
306 bones: in insulin-treated mice, bone glucose uptake increases in femurs, decreases in  
307 humeri and is unaltered in tibiae. In contrast, Zoch *et al* report that insulin stimulates <sup>18</sup>F-  
308 FDG uptake into whole femurs and tibiae (Zoch et al., 2016). This discrepancy may relate  
309 to technical differences: Zoch *et al* analysed whole bones (including BM) of anaesthetised  
310 mice, whereas we distinguished between bone and BM and avoided anaesthesia. It is  
311 unclear why insulin is associated with decreased glucose uptake in humeral bone and BM;  
312 this is unlikely to be a technical issue given that we see expected insulin-stimulated glucose  
313 uptake in the heart, WAT and femur. Thus, the lack of increases in humeri and tibiae  
314 suggests that there are site-specific differences in skeletal insulin responsiveness.

315

316 Another major finding is that BMAT is molecularly and functionally distinct to brown and  
317 beige adipose tissues, both for cBMAT of mice and rabbits, and for rBMAT of humans at  
318 multiple skeletal sites. These molecular distinctions are consistent with several other  
319 studies. We and others previously found that tibial *Ucp1* expression is over 10,000-fold lower  
320 than in BAT (Krings et al., 2012; Sulston et al., 2016), consistent with our present finding  
321 that *Ucp1* is undetectable in whole mouse bones. Similarly, microarrays show that *UCP1* is  
322 not enriched in whole BM of mice or humans (Dezso et al., 2008; Thorrez et al., 2008), nor  
323 is it greater in BMAds vs white adipocytes of mice (Liu et al., 2011). Moreover, BMAd  
324 progenitors are more white-like than brown-like and do not express brown adipocyte

325 markers after adipogenesis *in vitro* (Ambrosi et al., 2017). However, despite these diverse  
326 lines of evidence to the contrary, the concept that BMAT may be BAT- or beige-like has  
327 persisted. Thus, our *in vivo* functional analyses of mice and humans are a key advance  
328 because they confirm that cold exposure does not induce glucose uptake or beiging in  
329 BMAT. This demonstrates, conclusively, that BMAT is not BAT- or beige-like.

330  
331 Our glucocorticoid studies provide further insights. Unlike in BAT, acute glucocorticoid  
332 treatment in humans does not stimulate glucose uptake in BMAT; however, it does influence  
333 uptake across lumbar vertebrae, with a trend for increases in RM (Fig. S4E). It is notable  
334 that this occurs only in vertebrae, because these are also the bones in which glucocorticoids  
335 drive the greatest increases in fracture risk (Briot and Roux, 2015). This raises the possibility  
336 that glucocorticoids modulate BM and bone metabolism in a site-specific manner and that  
337 these metabolic effects contribute to glucocorticoid-induced osteoporosis. Future studies  
338 using different doses and durations of glucocorticoids would further elucidate their ability to  
339 modulate metabolism of RM, BMAT and bone, and whether this influences glucocorticoid-  
340 induced osteoporosis.

341  
342 Although BMAT glucose uptake is not stimulated by insulin at physiological concentrations,  
343 cold exposure or glucocorticoids, a major finding is that BMAT in humans has high basal  
344 glucose uptake, exceeding that of WAT and greater than that for bone or RM in the axial  
345 skeleton. Superficially, this seems at odds with two studies reporting that BM <sup>18</sup>F-FDG  
346 uptake correlates inversely with BM fat content (Huovinen et al., 2014; Schraml et al., 2015);  
347 however, on further consideration, it is clear that these findings are not inconsistent with  
348 ours. Indeed, we show that axial bones have less BMAT but greater BM <sup>18</sup>F-FDG uptake  
349 than humeri or femurs, mirroring these and other previous reports of <sup>18</sup>F-FDG uptake in  
350 whole BM (Huovinen et al., 2016). Importantly, unlike our approach, no previous studies  
351 have distinguished <sup>18</sup>F-FDG uptake between RM and BMAT specifically. Thus, a unique  
352 advance of our work is the finding that, in axial bones, BMAT glucose uptake is greater than  
353 in bone and similar or greater than in RM. This is particularly notable given that both BM and  
354 bone are sites of high glucose uptake, capable of exceeding levels observed in WAT or  
355 skeletal muscle (Huovinen et al., 2016; Huovinen et al., 2014; Zoch et al., 2016) (Fig. 4, Fig.  
356 S4). Indeed, bone glucose uptake is required for normal metabolic function (Li et al., 2016).  
357 Together, these observations support the conclusion that BMAT may influence systemic  
358 glucose homeostasis.

359  
360 We also reveal that BMAT glucose uptake varies at different skeletal sites, generally being  
361 greater in axial BMAT compared to BMAT in long bones. This is consistent with depot-  
362 dependent differences in other BMAT characteristics and, broadly, with the concept that  
363 BMAT exists in regulated and constitutive subtypes (Craft et al., 2018). However, while axial  
364 BMAT has higher glucose uptake, BMAT volume in peripheral bones is typically far higher  
365 (Fig. 4, Fig. S4) (Kricun, 1985). Thus, the systemic metabolic influence of axial BMAT may  
366 be greater in conditions such as ageing, obesity, osteoporosis or caloric restriction, in which  
367 axial BMAT accumulates (Scheller et al., 2016).

368  
369 Why does BMAT have such high basal glucose uptake? This may result from BMAdS having  
370 high expression of *SLC2A1* and/or *SLC2A3* (Fig. 1), a finding supported by previous  
371 microarray studies (Liu et al., 2011). Indeed, among numerous human tissues, *SLC2A3*  
372 expression is highest in BM (Dezso et al., 2008), while *Slc2a3* is also greater in BM than in  
373 WAT of mice (Thorrez et al., 2008). Mouse BMAdS also have a dense mitochondrial network  
374 (Robles et al., 2018) and, by electron microscopy, we found that mitochondria are also  
375 abundant in human BMAdS (S. Cinti, personal communication). This supports the conclusion

376 that BMADs are metabolically active, which may further explain their high basal glucose  
377 uptake.

378  
379 Finally, we have developed a method to identify BMAT from CT scans, allowing its functional  
380 analysis by PET/CT. At least one other study has used HU thresholding to try to distinguish  
381 BMAT-enriched vs BMAT-deficient BM (Rantalainen et al., 2013), but our method is more  
382 comprehensive because we directly compared paired MRI and CT scans to identify the  
383 optimal BMAT HU thresholds. The finding that the sternum is BMAT-rich was unexpected  
384 as this contrasts with most other axial bones; however, it is consistent with adipogenic  
385 progenitors being readily detectable within sternal BM (Ambrosi et al., 2017). Otherwise, our  
386 method identifies site- and age-dependent differences in RM and BMAT that are in full  
387 agreement with previous studies (Baum et al., 2018; Kricun, 1985; Schraml et al., 2015).  
388 Applying our PET/CT approach to other clinical and preclinical studies, including  
389 retrospectively, therefore holds great promise to reveal further physiological and  
390 pathological roles of BMAT. Importantly, the diversity of PET tracers could extend such  
391 studies far beyond glucose metabolism, allowing many other functions of BMAT to be  
392 addressed.

393  
394 In summary, this study is the first to dissect BMAT glucose metabolism *in vivo* and identifies  
395 BMAT as a distinct, major subtype of adipose tissue.

395 **ACKNOWLEDGEMENTS**

396

397 This work was supported by grants from the Medical Research Council (MR/M021394/1 to  
398 W.P.C.; MR/K010271/1 to R.H.S.), the National Institutes of Health (R01 DK62876 and R24  
399 DK092759 to O.A.M.; K99-DE024178 to E.L.S.; and P30 DK089503 to the Michigan  
400 Nutrition Obesity Research Center), the Wellcome Trust-University of Edinburgh Institutional  
401 Strategic Support Fund (to W.P.C. and K.J.S.), and the British Heart Foundation (4-year  
402 BHF PhD Studentship to R.J.S., B.J.T., M.C.S. and B.M.N; BHF CoRE Bioinformatics Grant  
403 to W.P.C.; BHF CoRE grant to A.J.D.). W.P.C. is further supported by a Chancellor's  
404 Fellowship from the University of Edinburgh. A.A.S.T was funded by the British Heart  
405 Foundation (RG/16/10/32375). E.J.R.v.B is supported by SINAPSE (the Scottish Imaging  
406 Network). We are grateful to the British Heart Foundation for providing funding towards  
407 establishment of the Edinburgh Preclinical PET/CT laboratory (RE/13/3/30183), and to NHS  
408 Research Scotland (NRS) for financial support of the Edinburgh Clinical Research Facility.  
409 R.H.S and M.C.W. are supported by The Chief Scientist Office of the Scottish Government  
410 (SCAT/17/02 to R.H.S.; PCL/17/04 to M.C.W.). J.P.M.A is supported by BHF Clinical  
411 Research Training Fellowship no. FS/17/51/33096. We are grateful to John Henderson  
412 (BVS, University of Edinburgh) for support with mouse husbandry; Anish K. Amin  
413 (Department of Orthopaedic Surgery, Royal Infirmary Edinburgh), Beena Polouse and Frank  
414 Morrow (Edinburgh Clinical Research Facility,) for help with human studies; Tashfeen  
415 Walton and Christophe Lucatelli (Edinburgh Imaging, University of Edinburgh) for  
416 radiotracer production; Robert K. Semple (Centre for Cardiovascular Science, University of  
417 Edinburgh) for critical feedback on this manuscript; and to staff at the University of Michigan  
418 microarray core facility for processing of rabbit microarray data.

419 **AUTHOR CONTRIBUTIONS** (based on CRediT taxonomy)

420

421 **Conceptualisation**, K.J.S. and W.P.C.; **Methodology**, K.J.S., A.A.S.T, E.L.S., G.P., C.G.,  
422 L.E.R., W.A.M., A.J.D., A.P., S.C., R.J.W., O.A.M., N.M.M, R.H.S. and W.P.C.;  
423 **Investigation**, K.J.S., D.M., E.L.S., L.E.R., G.P., C.G., A.L., R.J.S., B.J.T., M.C.S., B.M.N.,  
424 C.J.A., D.S., G.J.M., M.R.D., J.P.M.A., M.C.W., R.J.W., E.J.R.v.B., R.H.S. and W.P.C.;  
425 **Formal Analysis**, K.J.S., A.A.S.T, D.M., E.L.S., G.P., C.G., W.A.M., J.P.M.A., M.C.W.,  
426 R.J.W., E.J.R.v.B., N.M.M., R.H.S. and W.P.C.; **Resources**, A.A.S.T, A.P., S.C., G.J.M.,  
427 M.R.D., J.P.M.A., M.C.W., E.J.R.v.B., N.M.M., R.H.S.; Writing – Original Draft, K.J.S. and  
428 W.P.C.; **Writing – Review & Editing**, K.J.S., A.A.S.T, E.L.S., G.P., W.A.M., A.J.D., S.C.,  
429 M.C.W., R.J.W., E.J.R.v.B., O.A.M., R.H.S, W.P.C.; **Visualisation**, K.J.S. and W.P.C.;  
430 Supervision, A.J.D., A.P., M.R.D., O.A.M., N.M.M., R.H.S. and W.P.C.; **Funding**  
431 **Acquisition**, A.J.D., O.A.M., N.M.M., R.H.S. and W.P.C.

432 **DECLARATION OF INTERESTS**

433 E.J.R.v.B. has received research support from Siemens Healthineers and is the owner of  
434 QCTIS Ltd.

435 **FIGURE TITLES AND LEGENDS**

436

437 **Figure 1 – BMAT is transcriptionally distinct to white, brown and beige adipose**  
438 **tissues. (A-D)** Transcriptional profiling of gonadal WAT, inguinal WAT, and whole BMAT  
439 isolated from the proximal tibia (pBMAT), distal tibia (dBMAT) or radius and ulna (ruBMAT)  
440 of two cohorts of rabbits. (A) Principal component analysis of both cohorts. (B-D) Volcano  
441 plots (B), GSEA (C) and heatmaps (D) of transcripts differentially expressed between BMAT  
442 (dBMAT + ruBMAT) and WAT (iWAT + gWAT) in rabbit cohort 1. In (B-E), red text indicates  
443 differentially expressed transcripts (B) or transcripts/pathways relating to glucose  
444 metabolism and/or insulin responsiveness (C-E); *ns* = not significant. **(E)** Transcriptional  
445 profiling of adipocytes isolated from femoral BM or subcutaneous WAT of humans. **(F)**  
446 Representative micrographs of H&E-stained sections of human femoral BM, subcutaneous  
447 WAT and trabecular bone; scale bar = 150  $\mu$ m. **(G)** qPCR (G) of adipocytes isolated from  
448 tissues in (G). Data are mean  $\pm$  SEM of the following numbers per group: BM Ads, *n* = 10;  
449 WAT Ads, *n* = 10; Bone Ads, *n* = 7 (*except IRS1, where n = 2 only*). For each transcript,  
450 significant differences between each cell type are indicated by \* (*P* < 0.05), \*\* (*P* < 0.01) or  
451 \*\*\* (*P* < 0.001). See also Figure S1 and Figure S2.

452

453 **Figure 2 – Insulin treatment in mice does not induce glucose uptake in BMAT.** Insulin-  
454 stimulated glucose uptake was assessed by PET/CT. **(A)** Blood glucose post-insulin or  
455 vehicle. **(B,D)** Representative PET/CT images of the torso (B) or legs (D) of vehicle- and  
456 insulin-treated mice; some  $^{18}$ F-FDG uptake into skeletal muscle is evident in the image of  
457 the vehicle-treated mouse (D), possibly resulting from physical activity. **(C)** Gamma counts  
458 of  $^{18}$ F-FDG uptake in iWAT and gWAT, shown as % injected dose per g tissue (%ID/g). **(E)**  
459 BMAT analysis by osmium tetroxide staining. BMAT is shown in red in representative  $\mu$ CT  
460 reconstructions and quantified as adipose volume relative to total BM volume (Ad.V/Ma.V).  
461 **(F)**  $^{18}$ F-FDG uptake in the indicated tissues was determined from PET/CT scans. Data are  
462 presented as mean  $\pm$  SEM of 5-6 mice (A,C,F) or 5-7 mice (E). Significant differences  
463 between control and insulin-treated samples are indicated by \* (*P* < 0.05), \*\* (*P* < 0.01) or \*\*\*  
464 (*P* < 0.001). In (E), groups do not significantly differ if they share the same letter.

465

466 **Figure 3 – Cold exposure does not induce glucose uptake or beiging in BMAT.** Cold-  
467 induced glucose uptake was assessed by PET/CT, as described in Figure S3A. **(A)**  
468 Representative PET/CT images of control, acute and chronic cold mice show increased  $^{18}$ F-  
469 FDG uptake in BAT but not tibiae; some  $^{18}$ F-FDG is evident in skeletal muscle of each group.  
470 **(B,C)**  $^{18}$ F-FDG uptake in the indicated tissues was determined by PMOD analysis of PET/CT  
471 scans (B) or gamma counting (C). **(D)** Representative micrographs of H&E-stained tissues,  
472 showing that cold exposure decreases lipid content in BAT and promotes beiging of iWAT,  
473 but these effects do not occur in BMAT; scale bar = 150  $\mu$ m. **(E-G)** Cold exposure induces  
474 brown and beige adipocyte transcripts in BAT and iWAT, but not in whole bones. *ND* = not  
475 detectable. Data in (B-C) and (E-G) are shown as mean  $\pm$  SEM of 7-8 mice per group.  
476 Significant differences between groups are indicated by # (*P* < 0.01), \* (*P* < 0.05), \*\* (*P* < 0.01)  
477 or \*\*\* (*P* < 0.001). See also Figure S3.

478

479 **Figure 4 – Human BMAT is functionally distinct to BAT and is a major site of basal**  
480 **glucose uptake. (A)** Representative MRI (HASTE) and CT images from one subject. **(B)**  
481 HU distribution of scWAT, BMAT-rich BM (sternum) and BMAT-deficient BM (vertebrae).  
482 Data are mean  $\pm$  SEM (*n* = 33). Thresholds diagnostic for BMAT (<115) and RM (115-300)  
483 are indicated by dashed lines. **(C)** CT images of a 32-year-old subject, highlighting BMAT  
484 or RM identified using the diagnostic thresholds in (B). Tibiae are shown for completeness  
485 but were not present in any other available CT scans. **(D,E)** PET/CT analysis of  $^{18}$ F-FDG  
486 uptake in *No BAT*, *Active BAT* and cold-exposed (*Cold*) subjects. Representative PET/CT

487 scans in (D) highlight the BM cavities of the vertebrae and sternum; arrows indicate  $^{18}\text{F}$ -  
488 FDG uptake in supraclavicular BAT. **(F,G)**  $^{18}\text{F}$ -FDG uptake in bone tissue, RM and BMAT  
489 (F), or BMAT and scWAT (G), of room-temperature subjects (*No Bat* and *Active BAT*  
490 groups); Fem. = femur, Hum. = humerus, Clav. = clavicle, Vert. = vertebrae, Stern. =  
491 sternum. Data are shown as mean  $\pm$  SEM (E), paired individual values (F) or box-and-  
492 whisker plots (G) of 8 (*No BAT*) or 7 (*7 Active BAT, Cold*) subjects per group. Significant  
493 differences between bone, RM and BMAT are indicated by \* ( $P < 0.05$ ), \*\* ( $P < 0.01$ ) or \*\*\*  
494 ( $P < 0.001$ ). Significant differences between *No BAT*, *Active BAT* and *Cold* groups are  
495 indicated by # ( $P < 0.05$ ) or ### ( $P < 0.001$ ). See also Figure S4.



496 **METHODS**

497 **Table of key resources**

REAGENT or RESOURCE	SOURCE	IDENTIFIER
<b>BIOLOGICAL SAMPLES</b>		
Human bone marrow ( <i>cohort 1</i> )	Orthopedic and Traumatology Department, Ospedali Riuniti, Ancona, Italy	N/A
Human white adipose tissue ( <i>cohort 1</i> )	Hepatobiliary and Abdominal Transplantation Surgery, Department of Experimental and Clinical Medicine, Università Politecnica delle Marche, Ancona, Italy	N/A
Human bone marrow and white adipose tissue ( <i>cohort 2</i> )	Edinburgh Adipose Tissue Biobank	N/A
<b>CHEMICALS</b>		
Collagenase Type I	Worthington Biochemicals	LS004196
18F-Fluorodeoxyglucose	Edinburgh Clinical Research Imaging Centre (Edinburgh, UK)	N/A
Insulin	Eli Lilly (Indianapolis, USA)	Humulin S
Ribozol™	Amresco (USA)	N580
Osmium Tetroxide	Agar Scientific (UK)	AGR1022
<b>OLIGONUCLEOTIDES</b>		
See Table 2	This paper	N/A
<b>EXPERIMENTAL MODELS: Organisms/Strains</b>		
Mouse: C57BL/6J	Charles River	027
Rabbit: New Zealand White	Envigo	HsdJf:NZW
<b>SOFTWARE</b>		
Prism	GraphPad	v8.1.0
Heatmapper	(Babicki et al., 2016)	<a href="http://www.heatmapper.ca/">http://www.heatmapper.ca/</a>
GSEA	(Subramanian et al., 2005).	v3.0 [build: 0160]
NRecon	Bruker microCT (Kontich, Belgium)	v1.6.9.4
CT Analyzer	Bruker microCT (Kontich, Belgium)	v1.13.5.1
PMOD	PMOD Technologies LLC (Zurich, Switzerland)	v3.806
Analyze	AnalyzeDirect (Overland Park, KS, USA)	v12.0
MatLab	Mathworks	R2018b
<b>OTHER</b>		
TSE Phenomaster	TSE	PhenoMaster 1.0 with software version 6.1.9
OneTouch Verio Glucometer	OneTouch	User's manual <a href="#">here</a>

Gamma counter	PerkinElmer (USA)	Wizzard <sup>2</sup>
Preclinical PET/CT scanner	Mediso (Budapest, Hungary)	nanoScan PET/CT 122S
Clinical PET/CT scanner	Siemens Medical Systems (Erlangen, Germany)	Biograph mCT
MRI scanner	Siemens Medical Systems (Erlangen, Germany)	3T Verio
Clinical CT scanner	Toshiba Medical Systems (Japan)	Aquilion ONE

499  
500  
501  
502  
503  
504  
505  
506  
507  
508  
509

## Human subjects

For human subjects in cohort 1 (Fig. 1E, Supplemental Fig. 2A-B), ethical approval and subject characteristics are as described previously (Mattiucci et al., 2018). For human subjects in cohort 2 (Fig. 1F-G, Supplemental Fig. 2C-D) and those undergoing MRI or PET/CT (Fig. 4, Supplemental Fig. 5-6), all studies were reviewed and approved by the South East Scotland Research Ethics Committee, with informed consent obtained from each subject. Characteristics for cold-exposed, placebo-treated and prednisolone-treated subjects are as described previously (Ramage et al., 2016b). Characteristics for all other subjects are provided below in Table 1.

Study	Number of Subjects (Male/Female)	Age	BMI	Diabetic	Osteoporotic
BMA <i>d</i> isolation	10 (4/6)	67.1 ± 5.9	31.6 ± 6.9	0%	0%
MRI & CT	33 (24/9)	65.7 ± 8.1	29.1 ± 4.8	ND	ND
Room temp (no BAT)	10 (2/8)	51.5 ± 19.6	20.7 ± 2.4	0%	ND
Room temp (active BAT)	10 (2/8)	51.1 ± 16.0	21.0 ± 2.2	0%	ND

510 **Table 1.** Characteristics of subjects in human cohort 2 (used for BMA*d* isolation and  
511 molecular analysis), those who underwent paired CT and MRI analysis (used to identify  
512 Hounsfield Units for BMAT), and those without or with detectable BAT at room  
513 temperature (Fig. 4, Supplemental Fig. 5-6). Age and BMI are mean ± SD. ND = not  
514 determined.

515

## Animals

516 Studies in New Zealand White rabbits were approved by the University of Michigan  
517 Committee on the Use and Care of Animals, with daily care overseen by the Unit for  
518 Laboratory Animal Medicine. Rabbit housing, monitoring and tissue isolation were done as  
519 described previously (Cawthorn et al., 2016). For cohort 1 (Fig. 1), male rabbits (3.14 ± 0.19  
520 kg, mean ± SD) were fed a high-fiber diet (cat. No 5326, LabDiet), receiving 100 g/day (31.91  
521 ± 0.19 g/kg body mass/day; mean ± SD) until 22 weeks of age. For cohort 2 (Supplemental  
522 Fig. 1), male rabbits were fed the same high-fiber diet *ad libitum* (68.26 ± 4.82 g/kg body  
523 mass/day; mean ± SD) until 13 weeks of age. Rabbits in each cohort were then euthanized  
524 and tissues isolated for subsequent analysis.  
525

526

527 Studies in C57BL/6JCrI mice were approved by the University of Edinburgh Animal Welfare  
528 and Ethical Review Board and were done under project licenses granted by the UK Home

528 Office. Male C57BL/6J mice were bred in-house and housed on a 12 h light/dark cycle with  
529 free access to water and food, as indicated.  
530

### 531 **Human cell and tissue isolation**

532 For cohort 1, adipocytes were isolated from femoral head bone marrow (BMAds) or  
533 subcutaneous WAT (WAT Ads) as described previously (Mattiucci et al., 2018). For cohort  
534 2, adipocytes from bone marrow, trabecular bone and WAT were isolated from patients  
535 undergoing hip-replacement surgery: BMAds were obtained from the proximal femoral  
536 diaphysis; trabecular bone adipocytes were from the proximal femoral metaphysis; and WAT  
537 Ads were from gluteofemoral subcutaneous WAT. Immediately after surgical isolation,  
538 tissues were washed and stored in ice-cold Dulbecco's phosphate-buffered saline (DPBS,  
539 14190250, Gibco) for transport to a sterile tissue culture hood. Therein, DPBS was decanted  
540 through a sterile 300 µm nylon filter to remove blood, lipid and small debris. The remaining  
541 washed tissue was then transferred to a sterile, pre-weighed petri dish (100 mm) and tissue  
542 mass recorded. A solution of collagenase type I (Worthington Biochemicals) was made at 1  
543 mg/mL in Krebs-Ringer HEPES (KRH) buffer (120 mM NaCl, 2 mM KCl, 1 mM KH<sub>2</sub>PO<sub>4</sub>, 0.6  
544 mM MgSO<sub>4</sub>, 1 mM CaCl<sub>2</sub>\*2H<sub>2</sub>O, 82 mM HEPES, 5.5 mM D-Glucose, 1% BSA) pre-warmed  
545 to 37°C; sufficient volume was made to allow for 2 mL per mg tissue and the solution was  
546 passed through a 0.22 µm filter before use.  
547

548 After weighing, each tissue was minced in the petri dish using a sterile scalpel and scissors,  
549 then transferred to a Falcon tube containing the collagenase solution. Tissues in  
550 collagenase were then incubated for 45 min in a shaking water bath (120 rpm) at 37°C. Next,  
551 collagenase-digested tissue was passed through a 300 µm nylon filter and the cells within  
552 the filtrate were washed with fresh KRH buffer. Samples were then centrifuged at 500 rcf for  
553 5 min at 4°C. The floating adipocyte layer was transferred by pipette to a new tube to be  
554 used for RNA isolation; an aliquot was also analyzed histologically to confirm the presence  
555 of adipocytes. After aspirating and discarding the supernatant, the stromal vascular fraction  
556 (SVF) of cells within the pellet was resuspended in 2x volume of red blood cell lysis buffer  
557 (Cat. No. R7757, Sigma) and incubated at room temperature for 5 min to lyse erythrocytes.  
558 KRH buffer was added to bring the volume to 15 mL and samples were centrifuged at 700  
559 rcf for 10 min at 4°C. The SVF pellet was then used for RNA isolation.  
560

### 561 **RNA isolation and reverse transcription**

562 For human cohort 1, RNA was extracted as described previously (Mattiucci et al., 2018). For  
563 human cohort 2 and mouse studies, RNA was isolated from cells or tissues using Ribozol™  
564 solution (cat. No. N580, Amresco, USA,) according to the manufacturer's protocol. For rabbit  
565 studies, RNA was isolated from tissues as described previously (Cawthorn et al., 2016).  
566 Tissues included iWAT, gWAT, dBMAT and ruBMAT of both cohorts, and pBMAT of rabbit  
567 cohort 2. RNA was quantified using a NanoDrop spectrophotometer (Thermo Scientific,  
568 USA), and cDNA was synthesized using the Taqman® High Capacity cDNA Reverse  
569 Transcriptase Kit (Applied Biosystems, USA, cat. no. N8080234), in accordance with the  
570 manufacturer's guidelines.  
571

### 572 **Microarray analyses**

573 For human cohort 1, RNA extraction, generation of single-strand biotinylated cDNA, and  
574 hybridization to Human GeneChip® HTA 2.0 Arrays (Affymetrix) were done as described  
575 previously (Mattiucci et al., 2018). Transcripts were considered to be significantly  
576 differentially expressed between BMAds and WAT Ads when they had an adjusted *p*-value  
577 of 0.05 or less; *p*-values were adjusted for multiple comparisons using the Benjamini and  
578 Hochberg approach to control for false discovery rate (Benjamini and Hochberg, 1995).

579

580 For rabbit studies, purified RNA was digested on-column with DNase I and cleaned using  
581 the Qiagen RNeasy kit (Qiagen, Valencia, CA, USA) as recommended by the manufacturer.  
582 Total RNA was then submitted to the microarray core at the University of Michigan. The  
583 samples were screened for quality and processed in the microarray facility using custom  
584 rabbit Affymetrix arrays and the IVT Express kit (Affymetrix, Santa Clara, CA, USA). As a  
585 QC measure, the distribution of probe intensities and the 5' to 3' degradation profiles were  
586 checked to be consistent across samples. The core's statistician used RMA, from the Affy  
587 package of Bioconductor, to fit  $\log_2$  expression values to the data (Irizarry et al., 2003).  
588 Weighted, paired, linear models were then fit and contrast computed using the limma  
589 package (Smyth, 2004). Weighting was done using a gene-by-gene algorithm designed to  
590 down-weight chips that were deemed less reproducible (Ritchie et al., 2006). Probe-sets  
591 with a variance over all samples less than 0.05 were filtered out. Of the remainder, probe-  
592 sets with a  $\log_2$ -fold change of 2 or greater and an adjusted p-value of 0.05 or less were  
593 retained. P-values were adjusted for multiple comparisons using the Benjamini and  
594 Hochberg false discovery rate approach (Benjamini and Hochberg, 1995). Affy, affyPLM,  
595 and limma packages of Bioconductor, implemented in the R-statistical environment were  
596 used to analyze the data, including PCA analysis (Irizarry et al., 2003).

597

598 Pathways enriched in BMAT (combined dBMAT and ruBMAT) or WAT (combined iWAT and  
599 gWAT) of rabbits, or in isolated adipocytes from femoral BM and gluteofemoral scWAT  
600 (humans), were identified using Gene Set Enrichment Analysis (GSEA) software and the  
601 Molecular Signature Database (MSigDB) (Subramanian et al., 2005). For rabbits, pBMAT  
602 was not included in these analyses because it contained a high proportion of red marrow  
603 and therefore represented a less pure BMAT sample (Cawthorn et al., 2016). To ensure  
604 maximum compatibility with this software, rabbit gene identifiers were first converted to their  
605 corresponding human homologues using the BetterBunny algorithm (Craig et al., 2012).  
606 Volcano plots and heat maps (*Pearson Distance*) to visualize significantly differentially  
607 expressed transcripts (adjusted *p*-value <0.05, fold-change >2) were generated using Prism  
608 8 (GraphPad) and Heatmapper software (Babicki et al., 2016), respectively.

609

## 610 **qPCR**

611 For human cohort 2 and tissues from mice, reverse transcription, primer design/validation  
612 and qPCR were done as described previously (Sulston et al., 2016). Expression of each  
613 target gene was normalized to expression of 18S rRNA (human gene, *RNA18SN5*; mouse  
614 gene, *Rn18s*), *IPO8* or *Ppia*, based on consistency of housekeeper expression across all  
615 samples. For each transcript, expression is presented relative to the group with the highest  
616 expression. A Taqman assay was used to analyze *Ucp1* expression in mouse tissues  
617 (Thermo Fisher, Mm01244861\_m1). All other primer sequences are described in Table 2.

618

## 619 **Histology**

620 Fixed murine and human soft tissue and decalcified bones (14% EDTA for 14 days) were  
621 paraffin embedded by the histology core at The University of Edinburgh's Shared University  
622 Research Facilities (SuRF). Paraffin-embedded tissue sections were then sectioned at 100  
623  $\mu\text{m}$  intervals using a Leica RM2125 RTS microtome and collected onto 76 x 26 mm StarFrost  
624 slides (VWR, UK). The slides were baked at 37°C overnight before Hemotoxylin and Eosin  
625 (H&E) staining.

626

627

628

629

Species	Transcript	Forward Primer (5'-3')	Reverse Primer (5'-3')
<i>H. Sapiens</i>	<i>ADIPOQ</i>	TCCTCACTTCCATTCTGACTGC	GTAGAACAGCTCCCAGCAACA
	<i>CPT1B</i>	CTGGTGCTCAAGTCATGGTG	CTGCCTGCACGTCTGTATTC
	<i>INSR</i>	TAGACGTCCCGTCAAATATTGC	GAAGAAGCGTAAAGCGGTCC
	<i>IPO8</i>	TTTCCCCTCAAATGTGGCAGC	CTTCTCCTGCATCTCCACATAGT
	<i>IRS1</i>	AGAGGACCGTCAGTAGCTCA	TCTTCATGACACGGTGGTG
	<i>IRS2</i>	CACCTACGCCAGCATTGACT	GAAACAGTGCTGAGCGTCTTC
	<i>METRNL</i>	CCACAGGCTTCCAGTACGAG	TCAGGCTCGTGGGTAAGTTG
	<i>PPARG</i>	TCATGCTTGTGAAGGATGCAAG	ATCCCCACTGCAAGGCATTT
	<i>PRDM16</i>	GAGGAGAGAGATTCCGCGAG	CCCGGTTGGGCTCATAAT
	<i>RNA18SN5</i>	CGATGCTCTTAGCTGAGTGT	GGTCCAAGAATTTACCTCT
	<i>SLC2A1</i>	TCCCTGCAGTTTGGCTACAA	CAGGATGCTCTCCCCATAGC
	<i>SLC2A3</i>	TAGATTACAGCGATGGGGACAC	GTAGCCAAATTGGAAAGAGCCG
	<i>SLC2A4</i>	TCGGGCTTCCAACAGATAGG	GTTGTACCCAACTGCAGGG
	<i>TGM2</i>	GGAGTATGTCTCACCCAGC	CGTTCTTCAGGAAGTTGGGGT
<i>UCP1</i>	GTGTGCCCAACTGTGCAATG	ACGTTCCAGGATCCAAGTCG	
<i>M. musculus</i>	<i>Cpt1b</i>	TGTCTACCTCCGAAGCAGGA	CGGCTTGATCTCTTCACGGT
	<i>Dio2</i>	TCTTCCTGGCGCTCTATGAC	ACCACACTGGAATTGGGAGC
	<i>Ppara</i>	CCTGAACATCGAGTGTGCAATAT	TCTTCTTCTGAATCTTGCAGCT
	<i>Pparg</i>	GGAAAGACAACGGACAAATCAC	TACGGATCGAACTGGCAC
	<i>Ppia</i>	CACCGTGTTCTTCGACATCA	CAGTGCTCAGAGCTCGAAAGT
	<i>Prkaa1</i>	ACCAGGTCATCAGTACACCATC	ACACCGGAAAGGATCTGCTG
	<i>Rn18s</i>	CGATGCTCTTAGCTGAGTGT	GGTCCAAGAATTTACCTCT
	<i>Slc2a4</i>	ACTCATTCTTGGACGGTTCCTC	CACCCCGAAGATGAGTGGG

**Table 2.** Sequences of primers used for qPCR.

### Mouse insulin-treatment studies

C57BL/6J male mice aged ~16 weeks were fasted for 4 h at room temperature (RT). Insulin (Humulin S, Eli Lilly; 0.75 mIU/g body mass) or sterile saline (0.9%) was then administered to mice via intraperitoneal injection immediately prior to <sup>18</sup>F-FDG injection. Mice were then returned to their cages. At 0 min (just before <sup>18</sup>F-FDG injection), 15- and 60-min post-<sup>18</sup>F-FDG blood glucose was measured by tail venesection and blood sampled directly into EDTA-microtubes (Sarstedt, Leicester, UK). Mice were then anaesthetised and <sup>18</sup>F-FDG distribution assessed by PET/CT. After PET/CT, mice were sacrificed by overdose of anaesthetic. BAT, iWAT, gWAT, pWAT, mWAT, gonads, brain, kidneys, liver, spleen, pancreata, heart, soleus, gastrocnemius, femur, tibiae, humeri, and tail vertebrae were then dissected and <sup>18</sup>F-FDG uptake into each tissue was determined using a gamma counter (PerkinElmer). Counts per minute were converted to MBq activity using a standard conversion factor calibrated for the gamma counter. MBq were then corrected for radioactive decay based on the time of <sup>18</sup>F-FDG administration and the time of gamma counting. Finally, the corrected MBq values were normalized to the mass of each tissue. The final gamma counts are therefore presented as % injected dose per g tissue (%ID/g). Frozen and fixed

648 tissues were analyzed separately and the average MBq for each tissue was then calculated.  
649 Half of the dissected material was then snap frozen on dry ice and stored at -80°C for  
650 molecular analyses. The remaining half of the dissected material was placed into 10%  
651 formalin and stored at 4°C for histological analysis. PET/CT analysis was then done as  
652 described below.

653

### 654 **Mouse cold-exposure studies**

655 The protocol is adapted from (Wang et al., 2012), with a summary depicted in Supplemental  
656 Figure 3A. For the acute and chronic cold exposure studies (Fig. 3, Supplemental Fig. 4B-  
657 H), male C57BL/6J mice aged ~18 weeks were housed individually in TSE PhenoMaster  
658 cages for indirect calorimetry, monitoring of physical activity, and measurement of *ad libitum*  
659 food and water consumption. Mice in each group were first housed in these cages for 3 days  
660 at room temperature (RT) for acclimation and baseline measurements. Group 1 (*Control*)  
661 were then housed for 72 h at RT in standard cages; group 2 (*Acute cold*) for 68 h at RT in  
662 standard cages, followed by 4 h at 4°C in TSE cages; and group 3 (*Chronic cold*) for 72 h at  
663 4°C in TSE cages. Following TSE housing at 4°C, *Acute cold* and *Chronic cold* mice were  
664 returned to standard cages that had been pre-cooled on ice to 4 °C; *Control* mice continued  
665 to be housed in standard cages at RT. All groups were fasted, with access to water, for 4 h  
666 before administration of <sup>18</sup>F -FDG (such that *Acute cold* mice were fasted throughout their 4  
667 h cold exposure). Cages of cold-exposed mice were stored on ice in a ventilated cooler for  
668 transport to the PET/CT facility, while *Control* mice were transported at RT. After  
669 intraperitoneal injection of <sup>18</sup>F -FDG, mice were returned to cages at RT (*Control*) or 4°C  
670 (*Acute* and *Chronic cold*). At 0 min (just before <sup>18</sup>F -FDG injection), 15- and 60-min post-<sup>18</sup>F  
671 -FDG, blood glucose was measured by tail venesection. At 60-min post-<sup>18</sup>F -FDG, mice were  
672 placed under general anesthesia and underwent PET/CT imaging. Euthanasia, tissue  
673 isolation and gamma counting were done as described above for the insulin-treatment  
674 studies. PET/CT analysis was then done as described below.

675

676 To assess effects of cold exposure compared to mice housed at thermoneutrality, male  
677 C57BL/6J mice aged 12 weeks were individually housed for 48 h at 28°C, 22°C or 4°C. Each  
678 group was given AL access to chow diet throughout. Mice were then euthanised for tissue  
679 isolation.

680

### 681 **Mouse PET/CT analysis**

682 PET/CT scan images were reconstructed and data was analyzed using PMOD version 3.806  
683 (PMOD, Zurich, Switzerland). Standardised uptake values (SUV) were calculated for regions  
684 of interest, namely BAT, iWAT, gWAT; heart; bone tissue (without BM) from tibiae, femurs,  
685 and humeri; and the BM cavities within these bones. To distinguish bone tissue from BM, a  
686 calibration curve was generated using HU obtained from the acquisition of a CT tissue  
687 equivalent material (TEM) phantom (CIRS, model 091) and mouse CT scans. The TEM  
688 phantom consists of 2-4 mm hydroxyapatite rods representing mass densities of 1.08 to  
689 1.57 g/mL. The TEM-reconstructed CT image data was exported for analysis into PMOD  
690 and, for the extraction of TEM HU values, a VOI template was generated and placed on  
691 each rod (0.008mL for 2mm and 0.05mL 4mm). The calibration curve was plotted based on  
692 the calculated linear equation of the TEM HU values, in which the mouse tissue values were  
693 inserted/scaled. This ensured that, within whole bones, regions of interest were specific for  
694 bone or BM.

695

### 696 **Human PET/CT studies**

697 Subjects with active BAT at room temperature were identified retrospectively from clinical  
698 PET/CT scans; a control group, without detectable BAT, was then identified, ensuring that  
699 age, sex, weight, BMI and fasting blood glucose were matched to the active-BAT group. To

700 assess effects of cold exposure, subjects were exposed to a mild cold (16 °C) for 2 h, as  
701 described previously (Ramage et al., 2016b). To assess effects of prednisolone treatment,  
702 subjects were recruited to a double-blind, randomized crossover study, as described  
703 previously (Ramage et al., 2016b). All subjects were placed supine in a hybrid PET/CT  
704 scanner (Biograph mCT, Siemens Medical Systems) and scanned as described previously  
705 (Ramage et al., 2016b).  
706

#### 707 **Determination of attenuation density for BMAT in humans**

708 HU of subcutaneous fat, yellow marrow and red marrow were determined using Analyze  
709 12.0 software (AnalyzeDirect, Overland Park, KS, USA) based on data from 33 patients who  
710 had undergone paired CT and MRI scans (Table 1). The MRI sequence was an axial HASTE  
711 (Half Acquisition Single Shot Turbo Spin Echo) with a TE (echo time) of 50 ms, TR (repetition  
712 time) of 1000 ms, and slice thickness 8mm. BM fat corresponds to higher signal intensity  
713 compared to surrounding bone and muscle tissues, in HASTE MR techniques. CT scanning  
714 was performed as described previously (Williams et al., 2017). Using Analyze 12.0 software,  
715 the MR and CT scans were co-registered and volumes of interest were manually drawn  
716 around the sternum, vertebrae and subcutaneous adipose tissue. HU were extracted on a  
717 per voxel basis, and data underwent post-processing using Matlab to measure the total  
718 number of voxels across all patient HU (Fig. 4B), prior to ROC analysis (MedCalc). ROC  
719 analysis was then conducted on per voxel HU to determine threshold values with the  
720 greatest sensitivity and specificity to detect bone, yellow marrow and red marrow.  
721 Thresholds of above 300 HU were defined as bone regions, -200 to 115 HU as yellow  
722 marrow and 115 to 300 as red marrow.  
723

#### 724 **Micro-computed tomography scanning ( $\mu$ CT)**

725 Following euthanasia, murine tibiae were isolated, thoroughly cleaned and fixed in 10%  
726 formalin at 4°C for 48 hours. Bones were decalcified for 14 days in 14% EDTA and washed  
727 in Sorensen's phosphate buffer. Bones were then stained for 48 hours in 1% osmium  
728 tetroxide (Agar Scientific, UK), washed in Sorensen's phosphate buffer and embedded in  
729 1% agarose, forming layers of five tibiae arranged in parallel in a 30-mL universal tube.  
730 Tubes of embedded tibiae were then mounted in a Skyscan 1172 desktop micro CT (Bruker  
731 microCT, Kontich, Belgium). Samples were scanned through 360° using a step of 0.40°  
732 between exposures. A voxel resolution of 12.05  $\mu$ m was obtained in the scans using the  
733 following control settings: 54 kV source voltage, 185  $\mu$ A source current with an exposure  
734 time of 885 ms. A 0.5 mm aluminum filter and two-frame averaging were used to optimize  
735 the scan. After scanning, the data were reconstructed using NRecon v1.6.9.4 software  
736 (Bruker, Kontich, Belgium). The reconstruction thresholding window was optimized to  
737 encapsulate the target image. Volumetric analysis was performed using CT Analyzer  
738 v1.13.5.1 (Bruker microCT, Kontich, Belgium).  
739

#### 740 **Statistical analysis**

741 Microarray data were analyzed as described above. All other data were analyzed for normal  
742 distribution using the Shapiro-Wilk normality test. Normally distributed data were analyzed  
743 by ANOVA or t-tests, as appropriate. Where data were not normally distributed, non-  
744 parametric analyses were used. When appropriate, *P* values were adjusted for multiple  
745 comparisons. Data are presented as histograms or box and whisker plots. For the latter,  
746 boxes indicate the 25th and 75th percentiles; whiskers display the range; and horizontal  
747 lines in each box represent the median. All statistical analyses were performed using Prism  
748 software (GraphPad, USA). A *P*-value <0.05 was considered statistically significant.

## 749 SUPPLEMENTAL FIGURE LEGENDS

750

751

752 **Figure S1, Related to Figure 1 – BMAT is transcriptionally distinct to white, brown and**  
753 **beige adipose tissues.** Transcriptional profiling of WAT (gonadal + inguinal) vs whole  
754 BMAT (dBMAT + ruBMAT) from rabbit cohort 2. **(A)** Volcano plot of differentially expressed  
755 transcripts (FDR < 0.05, fold-change > 2). Transcripts characteristic of brown and/or beige  
756 adipocytes are labelled. Those with significant differential expression between WAT and  
757 BMAT are shown in red; those not differentially expressed are in grey. **(B)** Gene set  
758 enrichment analysis (GSEA) highlights lipid metabolism, glucose metabolism and insulin  
759 responsiveness as key pathways differentially regulated between WAT and BMAT.

760

761

762 **Figure S2, Related to Figure 1 – BM adipocytes in humans are transcriptionally**  
763 **distinct to those from WAT.** Transcriptional profiling (A,B) and qPCR analysis (C,D) of  
764 adipocytes isolated from the subcutaneous WAT or femoral diaphyseal BM of humans  
765 undergoing hip-replacement surgery. **(A,B)** Volcano plots (A) and heat maps (B) are  
766 presented as for Figures 1 and S1. **(C,D)** qPCR to validate purity of adipocytes isolated from  
767 each tissue (C) and showing that BM adipocytes generally do not have increased expression  
768 of brown or beige adipocyte markers (D). Transcript expression was normalised to  
769 expression of *IPO8* (C) or *RNA18SN5* (D). Data in (C) are mean  $\pm$  SEM of the following  
770 numbers per group: BM Ads, n = 8 (*ADIPOQ*) or 9 (*PPARG*); BM SVF, n = 3 (*ADIPOQ*) or  
771 5 (*PPARG*); WAT Ads, n = 10 (*ADIPOQ* and *PPARG*); WAT SVF, n = 5 (*ADIPOQ* and  
772 *PPARG*); Bone Ads and SVF, n = 7 (*PPARG*) or 3 (*ADIPOQ*). Data in (D) are mean  $\pm$  SEM  
773 of the following numbers per group: BM Ads, n = 3-10; WAT Ads, n = 6-10; Bone Ads, n =  
774 3-7. For each transcript, significant differences are indicated as for Figure 1.

774

775

776 **Figure S3, Related to Figure 3 – Effects of cold exposure on energy homeostasis and**  
777 **gene expression in BAT, iWAT and bone.** **(A)** Protocol for cold exposure and calorimetry  
778 studies, as described in the STAR Methods. **(B-H)** Effects of cold exposure on energy  
779 expenditure (B), body mass (C), baseline blood glucose (D), 72 h food intake (E) and  
780 transcript expression in BAT, iWAT or whole femurs (F-H). In (E), *Acute cold* mice are not  
781 shown because they were fasted throughout cold exposure. **(I)** A separate cohort of mice  
782 was housed at thermoneutrality, 22 °C or 4 °C for 48 h. Expression of BAT or beige cold  
783 exposure markers was then determined by qPCR of whole femurs. *ND* = not detectable. In  
784 (F-I), transcript expression was normalised to expression of *Rn18s* (F,H,I) or *Ppia* (G); the  
785 latter was used for iWAT because in this tissue *Rn18s*, but not *Ppia*, showed significant  
786 regulation between the three groups. Data are shown as box-and-whisker plots (B-E) or as  
787 mean  $\pm$  SEM (F-H) of 7-8 mice per group. In (I), data are mean  $\pm$  SEM of 8-10 mice per  
788 group. Significant differences between groups are indicated by \* ( $P < 0.05$ ), \*\* ( $P < 0.01$ ) or  
789 \*\*\* ( $P < 0.001$ ).

788

789

790 **Figure S4, Related to Figure 4 – PET/CT for identification and functional analysis of**  
791 **BMAT in humans.** **(A)** ROC analysis to identify HU thresholds to distinguish BMAT-rich  
792 (sternum) from BMAT-deficient (vertebrae) regions of BM. **(B)** Quantification of BMAT in CT  
793 scans of male and female subjects aged <60 or >60 years. A HU threshold of <115 was  
794 used to identify BMAT voxels in BM of the indicated bones, and total BM volume was also  
795 determined. The proportion of the BM cavity corresponding to BMAT (Ad.V/Ma.V) was then  
796 calculated. Data are shown as box-and-whisker plots of the following numbers of subjects  
797 for each group: <60 years, n = 28 (humerus), 9 (femur), or 27 (clavicle, sternum and  
798 vertebrae); >60 years, n = 7 for each bone. Significant differences between <60 and >60  
799 groups are indicated by \*\* ( $P < 0.01$ ). **(C)** Representative coronal PET/CT images of *No BAT*,  
800 *Active BAT* and *Cold* subjects.  $^{18}\text{F}$ -FDG uptake in BAT is evident in the *Active BAT* and *Cold*  
subjects (arrows). Femurs were not included in scans of the *Cold* group. **(D)**  $^{18}\text{F}$ -FDG uptake



801 in bone tissue, RM and BMAT of the indicated bones. Data are shown as mean  $\pm$  SEM of 8  
802 (*No BAT*) or 7 (7 *Active BAT*, *Cold*) subjects per group. Significant differences between  
803 these groups *No BAT*, *Active BAT* and *Cold* groups are indicated by # ( $P < 0.05$ ). **(E)**  
804 Subjects were treated with prednisolone or placebo control prior to analysis of  $^{18}\text{F}$ -FDG  
805 uptake by PET/CT. Data are shown as paired individual values for each subject. For each  
806 skeletal site, the influence of treatment or tissue (bone, RM, BMAT), and interactions  
807 between these, were determined by 2-way ANOVA;  $P$  values are shown beneath the graph.

## 808 REFERENCES

- 809 Abel, E.D., Peroni, O., Kim, J.K., Kim, Y.B., Boss, O., Hadro, E., Minnemann, T., Shulman, G.I.,  
810 and Kahn, B.B. (2001). Adipose-selective targeting of the GLUT4 gene impairs insulin action in  
811 muscle and liver. *Nature* *409*, 729-733.
- 812 Ambrosi, T.H., Scialdone, A., Graja, A., Gohlke, S., Jank, A.M., Bocian, C., Woelk, L., Fan, H.,  
813 Logan, D.W., Schurmann, A., et al. (2017). Adipocyte Accumulation in the Bone Marrow during  
814 Obesity and Aging Impairs Stem Cell-Based Hematopoietic and Bone Regeneration. *Cell Stem*  
815 *Cell* *20*, 771-784 e776.
- 816 Babicki, S., Arndt, D., Marcu, A., Liang, Y., Grant, J.R., Maciejewski, A., and Wishart, D.S. (2016).  
817 Heatmapper: web-enabled heat mapping for all. *Nucleic Acids Res* *44*, W147-153.
- 818 Baum, T., Rohrmeier, A., Syväri, J., Diefenbach, M.N., Franz, D., Dieckmeyer, M., Scharr, A.,  
819 Hauner, H., Ruschke, S., Kirschke, J.S., et al. (2018). Anatomical Variation of Age-Related  
820 Changes in Vertebral Bone Marrow Composition Using Chemical Shift Encoding-Based Water-  
821 Fat Magnetic Resonance Imaging. *Front Endocrinol* *9*, 141.
- 822 Benjamini, Y., and Hochberg, Y. (1995). Controlling the False Discovery Rate: A Practical and  
823 Powerful Approach to Multiple Testing. *Journal of the Royal Statistical Society. Series B*  
824 (Methodological) *57*, 289-300.
- 825 Briot, K., and Roux, C. (2015). Glucocorticoid-induced osteoporosis. *RMD Open* *1*, e000014.
- 826 Carvalho, E., Kotani, K., Peroni, O.D., and Kahn, B.B. (2005). Adipose-specific overexpression of  
827 GLUT4 reverses insulin resistance and diabetes in mice lacking GLUT4 selectively in muscle.  
828 *Am. J. Physiol. Endocrinol. Metab.* *289*, E551-561.
- 829 Cawthorn, W.P., Scheller, E.L., Learman, B.S., Parlee, S.D., Simon, B.R., Mori, H., Ning, X., Bree,  
830 A.J., Schell, B., Broome, D.T., et al. (2014). Bone Marrow Adipose Tissue Is an Endocrine  
831 Organ that Contributes to Increased Circulating Adiponectin during Caloric Restriction. *Cell*  
832 *Metab.* *20*, 368-375.
- 833 Cawthorn, W.P., Scheller, E.L., Parlee, S.D., Pham, H.A., Learman, B.S., Redshaw, C.M., Sulston,  
834 R.J., Burr, A.A., Das, A.K., Simon, B.R., et al. (2016). Expansion of Bone Marrow Adipose  
835 Tissue During Caloric Restriction Is Associated With Increased Circulating Glucocorticoids and  
836 Not With Hypoleptinemia. *Endocrinology* *157*, 508-521.
- 837 Chapman, J., and Vega, F. (2017). Incidental brown adipose tissue in bone marrow biopsy. *Blood*  
838 *130*, 952.
- 839 Cinti, S. (2018). Adipose Organ Development and Remodeling. *Compr Physiol* *8*, 1357-1431.
- 840 Craft, C.S., Li, Z., MacDougald, O.A., and Scheller, E.L. (2018). Molecular differences between  
841 subtypes of bone marrow adipocytes. *Curr Mol Biol Rep* *4*, 16-23.
- 842 Craig, D.B., Kannan, S., and Dombkowski, A.A. (2012). Augmented annotation and orthologue  
843 analysis for *Oryctolagus cuniculus*: Better Bunny. *BMC Bioinformatics* *13*, 84.
- 844 Dezso, Z., Nikolsky, Y., Sviridov, E., Shi, W., Serebriyskaya, T., Dosymbekov, D., Bugrim, A.,  
845 Rakhmatulin, E., Brennan, R.J., Guryanov, A., et al. (2008). A comprehensive functional  
846 analysis of tissue specificity of human gene expression. *BMC biology* *6*, 49.
- 847 Huovinen, V., Bucci, M., Lipponen, H., Kiviranta, R., Sandboge, S., Raiko, J., Koskinen, S.,  
848 Koskensalo, K., Eriksson, J.G., Parkkola, R., et al. (2016). Femoral Bone Marrow Insulin  
849 Sensitivity Is Increased by Resistance Training in Elderly Female Offspring of Overweight and  
850 Obese Mothers. *PLoS One* *11*, e0163723.
- 851 Huovinen, V., Saunavaara, V., Kiviranta, R., Tarkia, M., Honka, H., Stark, C., Laine, J., Linderborg,  
852 K., Tuomikoski, P., Badeau, R.M., et al. (2014). Vertebral bone marrow glucose uptake is  
853 inversely associated with bone marrow fat in diabetic and healthy pigs: [(18)F]FDG-PET and  
854 MRI study. *Bone* *61*, 33-38.

- 855 Irizarry, R.A., Hobbs, B., Collin, F., Beazer-Barclay, Y.D., Antonellis, K.J., Scherf, U., and Speed,  
856 T.P. (2003). Exploration, normalization, and summaries of high density oligonucleotide array  
857 probe level data. *Biostatistics* 4, 249-264.
- 858 Kricun, M.E. (1985). Red-yellow marrow conversion: its effect on the location of some solitary bone  
859 lesions. *Skeletal Radiol.* 14, 10-19.
- 860 Krings, A., Rahman, S., Huang, S., Lu, Y., Czernik, P.J., and Lecka-Czernik, B. (2012). Bone  
861 marrow fat has brown adipose tissue characteristics, which are attenuated with aging and  
862 diabetes. *Bone* 50, 546-552.
- 863 Li, Z., Frey, J.L., Wong, G.W., Faugere, M.C., Wolfgang, M.J., Kim, J.K., Riddle, R.C., and  
864 Clemens, T.L. (2016). Glucose Transporter-4 Facilitates Insulin-Stimulated Glucose Uptake in  
865 Osteoblasts. *Endocrinology* 157, 4094-4103.
- 866 Liu, L.F., Shen, W.J., Ueno, M., Patel, S., and Kraemer, F.B. (2011). Characterization of age-  
867 related gene expression profiling in bone marrow and epididymal adipocytes. *BMC Genomics*  
868 12, 212.
- 869 Mattiucci, D., Maurizi, G., Izzi, V., Cenci, L., Ciarlantini, M., Mancini, S., Mensa, E., Pascarella, R.,  
870 Vivarelli, M., Olivieri, A., et al. (2018). Bone marrow adipocytes support hematopoietic stem cell  
871 survival. *J. Cell. Physiol.* 233, 1500-1511.
- 872 Nishio, M., Yoneshiro, T., Nakahara, M., Suzuki, S., Saeki, K., Hasegawa, M., Kawai, Y., Akutsu,  
873 H., Umezawa, A., Yasuda, K., et al. (2012). Production of functional classical brown adipocytes  
874 from human pluripotent stem cells using specific hemopoietin cocktail without gene transfer.  
875 *Cell Metab.* 16, 394-406.
- 876 Qiang, G., Whang Kong, H., Xu, S., Pham, H.A., Parlee, S.D., Burr, A.A., Gil, V., Pang, J., Hughes,  
877 A., Gu, X., et al. (2016). Lipodystrophy and severe metabolic dysfunction in mice with adipose  
878 tissue-specific insulin receptor ablation. *Mol Metabol* 5, 480-490.
- 879 Ramage, L.E., Akyol, M., Fletcher, A.M., Forsythe, J., Nixon, M., Carter, R.N., van Beek, E.J.,  
880 Morton, N.M., Walker, B.R., and Stimson, R.H. (2016a). Glucocorticoids Acutely Increase Brown  
881 Adipose Tissue Activity in Humans, Revealing Species-Specific Differences in UCP-1  
882 Regulation. *Cell Metab.* 24, 130-141.
- 883 Ramage, Lynne E., Akyol, M., Fletcher, Alison M., Forsythe, J., Nixon, M., Carter, Roderick N.,  
884 van Beek, Edwin J., Morton, Nicholas M., Walker, Brian R., and Stimson, Roland H. (2016b).  
885 Glucocorticoids Acutely Increase Brown Adipose Tissue Activity in Humans, Revealing Species-  
886 Specific Differences in UCP-1 Regulation. *Cell Metabolism* 24, 130-141.
- 887 Rantalainen, T., Nikander, R., Heinonen, A., Cervinka, T., Sievanen, H., and Daly, R.M. (2013).  
888 Differential effects of exercise on tibial shaft marrow density in young female athletes. *J. Clin.*  
889 *Endocrinol. Metab.* 98, 2037-2044.
- 890 Ritchie, M.E., Diyagama, D., Neilson, J., van Laar, R., Dobrovic, A., Holloway, A., and Smyth, G.K.  
891 (2006). Empirical array quality weights in the analysis of microarray data. *BMC Bioinformatics* 7,  
892 261.
- 893 Robles, H., Park, S., Joens, M.S., Fitzpatrick, J.A.J., Craft, C.S., and Scheller, E.L. (2018).  
894 Characterization of the bone marrow adipocyte niche with three-dimensional electron  
895 microscopy. *Bone* 118, 89-98.
- 896 Rosell, M., Kaforou, M., Frontini, A., Okolo, A., Chan, Y.W., Nikolopoulou, E., Millership, S.,  
897 Fenech, M.E., MacIntyre, D., Turner, J.O., et al. (2014). Brown and white adipose tissues:  
898 intrinsic differences in gene expression and response to cold exposure in mice. *Am. J. Physiol.*  
899 *Endocrinol. Metab.* 306, E945-964.
- 900 Sakaguchi, M., Fujisaka, S., Cai, W., Winnay, J.N., Konishi, M., O'Neill, B.T., Li, M., Garcia-Martin,  
901 R., Takahashi, H., Hu, J., et al. (2017). Adipocyte Dynamics and Reversible Metabolic  
902 Syndrome in Mice with an Inducible Adipocyte-Specific Deletion of the Insulin Receptor. *Cell*  
903 *Metab.* 25, 448-462.

- 904 Scheller, E.L., Cawthorn, W.P., Burr, A.A., Horowitz, M.C., and MacDougald, O.A. (2016). Marrow  
905 Adipose Tissue: Trimming the Fat. *Trends Endocrinol Metab* 27, 392-403.
- 906 Scheller, E.L., Khandaker, S., Learman, B.S., Cawthorn, W.P., Anderson, L.M., Pham, H.A.,  
907 Robles, H., Wang, Z., Li, Z., Parlee, S.D., et al. (2018). Bone marrow adipocytes resist lipolysis  
908 and remodeling in response to beta-adrenergic stimulation. *Bone* 118, 32-41.
- 909 Schraml, C., Schmid, M., Gatidis, S., Schmidt, H., la Fougere, C., Nikolaou, K., and Schwenzer,  
910 N.F. (2015). Multiparametric analysis of bone marrow in cancer patients using simultaneous  
911 PET/MR imaging: Correlation of fat fraction, diffusivity, metabolic activity, and anthropometric  
912 data. *J. Magn. Reson. Imaging* 42, 1048-1056.
- 913 Smyth, G.K. (2004). Linear models and empirical bayes methods for assessing differential  
914 expression in microarray experiments. *Stat Appl Genet Mol Biol* 3, Article3.
- 915 Subramanian, A., Tamayo, P., Mootha, V.K., Mukherjee, S., Ebert, B.L., Gillette, M.A., Paulovich,  
916 A., Pomeroy, S.L., Golub, T.R., Lander, E.S., et al. (2005). Gene set enrichment analysis: a  
917 knowledge-based approach for interpreting genome-wide expression profiles. *Proc. Natl. Acad.  
918 Sci. U. S. A.* 102, 15545-15550.
- 919 Sulston, R.J., and Cawthorn, W.P. (2016). Bone marrow adipose tissue as an endocrine organ:  
920 close to the bone? *Horm Mol Biol Clin Investig* 28, 21-38.
- 921 Sulston, R.J., Learman, B.S., Zhang, B., Scheller, E.L., Parlee, S.D., Simon, B.R., Mori, H., Bree,  
922 A.J., Wallace, R.J., Krishnan, V., et al. (2016). Increased Circulating Adiponectin in Response to  
923 Thiazolidinediones: Investigating the Role of Bone Marrow Adipose Tissue. *Front Endocrinol* 7,  
924 128.
- 925 Svensson, P.A., Jernas, M., Sjöholm, K., Hoffmann, J.M., Nilsson, B.E., Hansson, M., and  
926 Carlsson, L.M. (2011). Gene expression in human brown adipose tissue. *Int. J. Mol. Med.* 27,  
927 227-232.
- 928 Thorrez, L., Van Deun, K., Tranchevent, L.C., Van Lommel, L., Engelen, K., Marchal, K., Moreau,  
929 Y., Van Mechelen, I., and Schuit, F. (2008). Using ribosomal protein genes as reference: a tale  
930 of caution. *PLoS One* 3, e1854.
- 931 Tran, M.A., Dang, T.L., and Berlan, M. (1981). Effects of catecholamines on free fatty acid release  
932 from bone marrow adipose tissue. *J. Lipid Res.* 22, 1271-1276.
- 933 Wang, X., Minze, L.J., and Shi, Z.Z. (2012). Functional imaging of brown fat in mice with 18F-FDG  
934 micro-PET/CT. *Journal of visualized experiments : JoVE DOI: 10.3791/4060.*
- 935 Williams, M.C., Mirsadraee, S., Dweck, M.R., Weir, N.W., Fletcher, A., Lucatelli, C., MacGillivray,  
936 T., Golay, S.K., Cruden, N.L., Henriksen, P.A., et al. (2017). Computed tomography myocardial  
937 perfusion vs (15)O-water positron emission tomography and fractional flow reserve. *Eur. Radiol.*  
938 27, 1114-1124.
- 939 Wu, J., Bostrom, P., Sparks, L.M., Ye, L., Choi, J.H., Giang, A.H., Khandekar, M., Virtanen, K.A.,  
940 Nuutila, P., Schaart, G., et al. (2012). Beige adipocytes are a distinct type of thermogenic fat cell  
941 in mouse and human. *Cell* 150, 366-376.
- 942 Zoch, M.L., Abou, D.S., Clemens, T.L., Thorek, D.L., and Riddle, R.C. (2016). In vivo radiometric  
943 analysis of glucose uptake and distribution in mouse bone. *Bone Res* 4, 16004.

# Figure 1

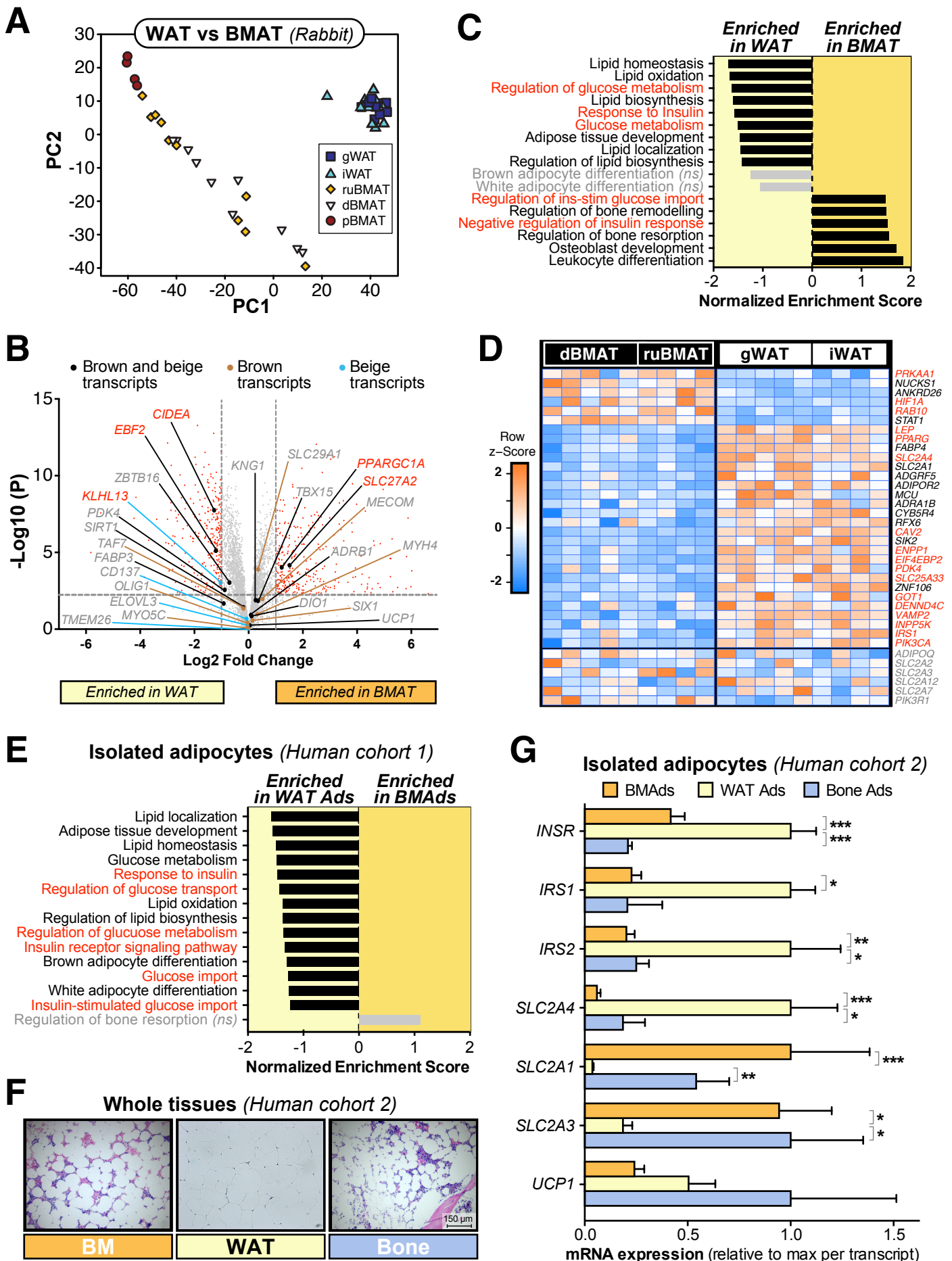


**Figure 1 – BMAT is transcriptionally distinct to white, brown and beige adipose tissues.** (A-D) Transcriptional profiling of gonadal WAT, inguinal WAT, and whole BMAT isolated from the proximal tibia (pBMAT), distal tibia (dBMAT) or radius and ulna (ruBMAT) of two cohorts of rabbits. (A) Principal component analysis of both cohorts. (B-D) Volcano plots (B), GSEA (C) and heatmaps (D) of transcripts differentially expressed between BMAT (dBMAT + ruBMAT) and WAT (iWAT + gWAT) in rabbit cohort 1. (E) Transcriptional profiling of adipocytes isolated from femoral BM or subcutaneous WAT of humans. In (B-E), red text indicates differentially expressed transcripts (B) or transcripts/pathways relating to glucose metabolism and/or insulin responsiveness (C-E); *ns* = not significant. (F) Representative micrographs of H&E-stained sections of human femoral BM, subcutaneous WAT and trabecular bone; scale bar = 150  $\mu$ m. (G) qPCR of adipocytes isolated from tissues in (F). Data are mean  $\pm$  SEM of the following numbers per group: BM Ads, *n* = 10; WAT Ads, *n* = 10; Bone Ads, *n* = 7 (except *IRS1*, where *n* = 2 only). For each transcript, significant differences between each cell type are indicated by \* (*P* <0.05), \*\* (*P* <0.01) or \*\*\* (*P* <0.001). See also Figure S1 and Figure S2.

## Figure 2

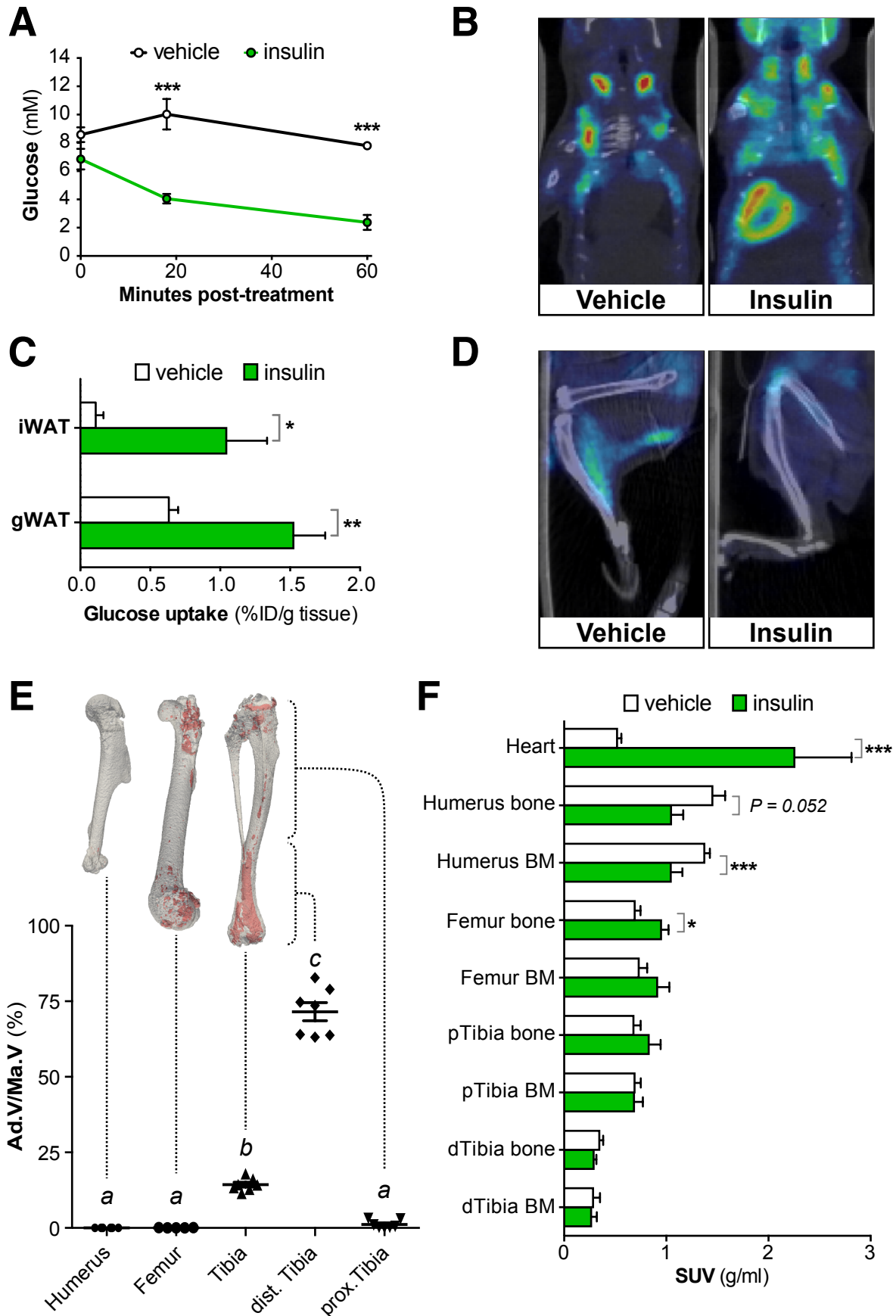


**Figure 2 – Insulin treatment in mice does not induce glucose uptake in BMAT.**

Insulin-stimulated glucose uptake was assessed by PET/CT. **(A)** Blood glucose post-insulin or vehicle. **(B,D)** Representative PET/CT images of the torso (B) or legs (D) of vehicle- and insulin-treated mice; some FDG uptake into skeletal muscle is evident in the image of the vehicle-treated mouse (D), possibly resulting from physical activity. **(C)** Gamma counts of FDG uptake in iWAT and gWAT, shown as % injected dose per g tissue (%ID/g). **(E)** BMAT analysis by osmium tetroxide staining. BMAT is shown in red in representative  $\mu$ CT reconstructions, and quantified as adipose volume relative to total BM volume (Ad.V/Ma.V). **(F)** FDG uptake in the indicated tissues was determined from PET/CT scans. Data are presented as mean  $\pm$  SEM of 5-6 mice (A,C,F) or 5-7 mice (E). Significant differences between control and insulin-treated samples are indicated by \* ( $P < 0.05$ ), \*\* ( $P < 0.01$ ) or \*\*\* ( $P < 0.001$ ). In (E), groups do not significantly differ if they share the same letter.



## Figure 3

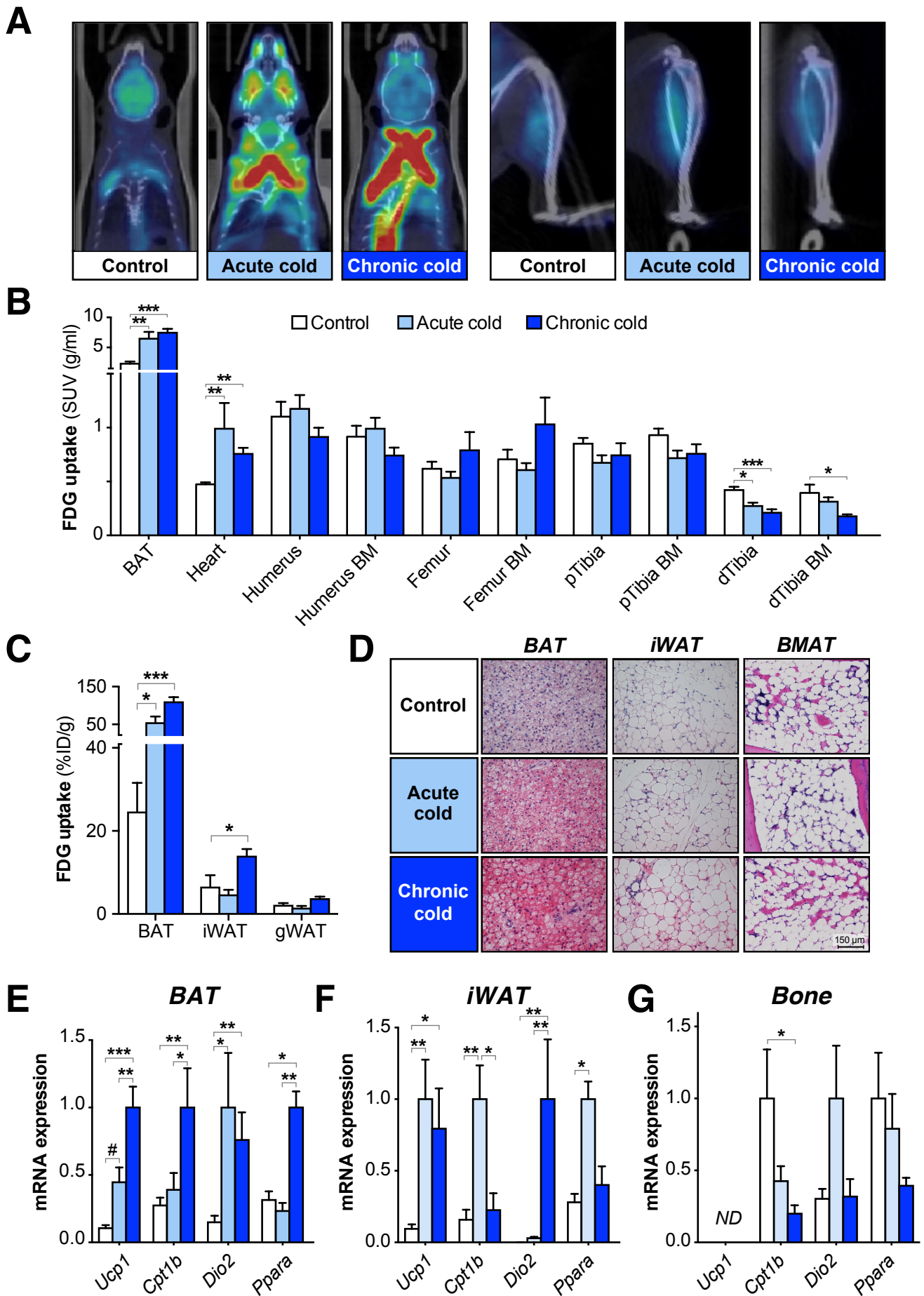


**Figure 3 – Cold exposure does not induce glucose uptake or beiging in BMAT.** Cold-induced glucose uptake was assessed by PET/CT, as described in Figure S4A. **(A)** Representative PET/CT images of control, acute and chronic cold mice show increased FDG uptake in BAT but not tibiae; some FDG is evident in skeletal muscle of each group. **(B,C)** FDG uptake in the indicated tissues was determined by PMOD analysis of PET/CT scans (B) or gamma counting (C). **(D)** Representative micrographs of H&E-stained tissues, showing that cold exposure decreases lipid content in BAT and promotes beiging of iWAT, but these effects do not occur in BMAT; scale bar = 150  $\mu$ m. **(E-G)** Cold exposure induces brown and beige adipocyte transcripts in BAT and iWAT, but not in whole bones. *ND* = not detectable. Data in (B-C) and (E-G) are shown as mean  $\pm$  SEM of 7-8 mice per group. Significant differences between groups are indicated by # ( $P < 0.01$ ), \* ( $P < 0.05$ ), \*\* ( $P < 0.01$ ) or \*\*\* ( $P < 0.001$ ). See also Figure S3.

## Figure 4

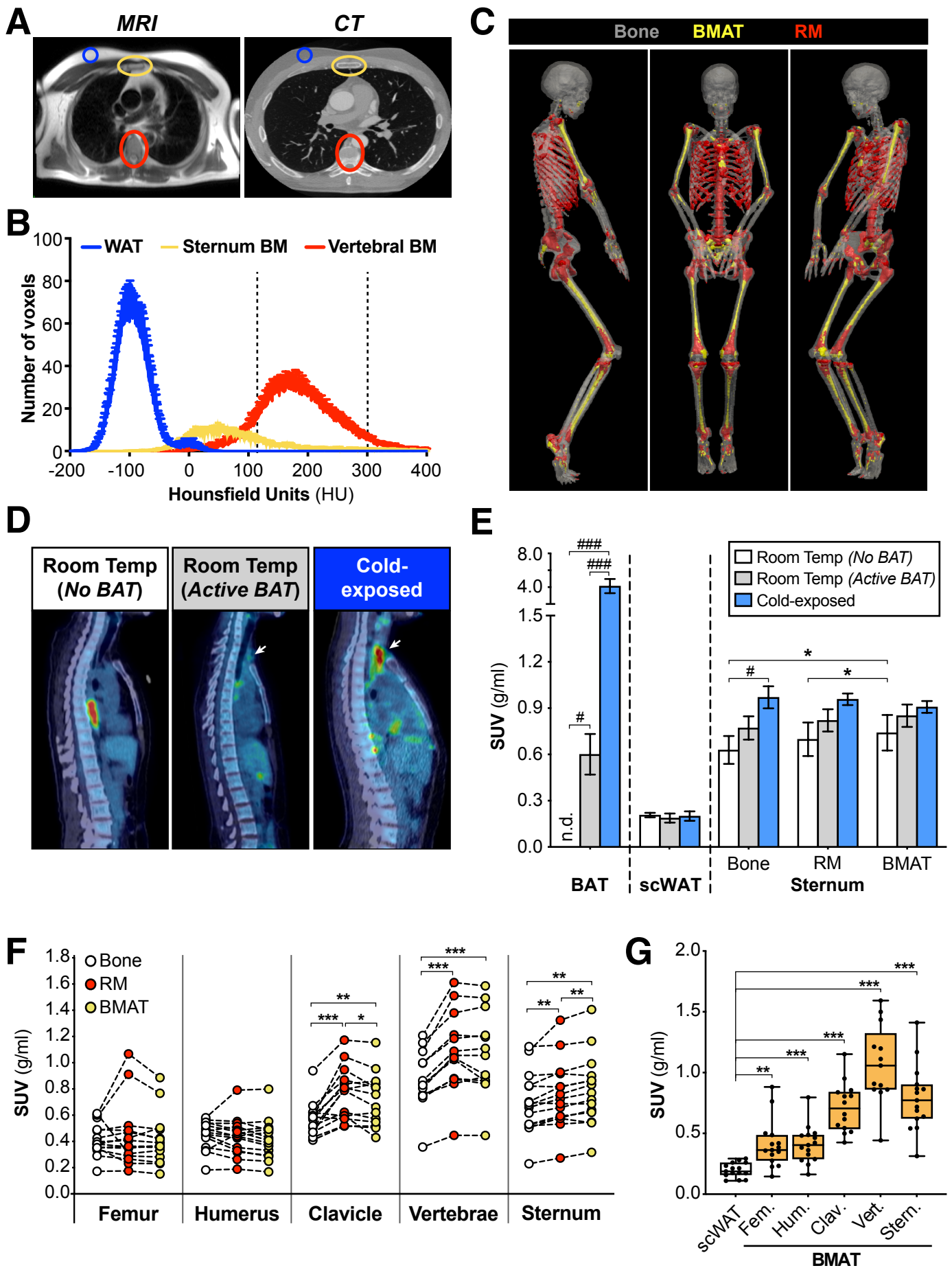
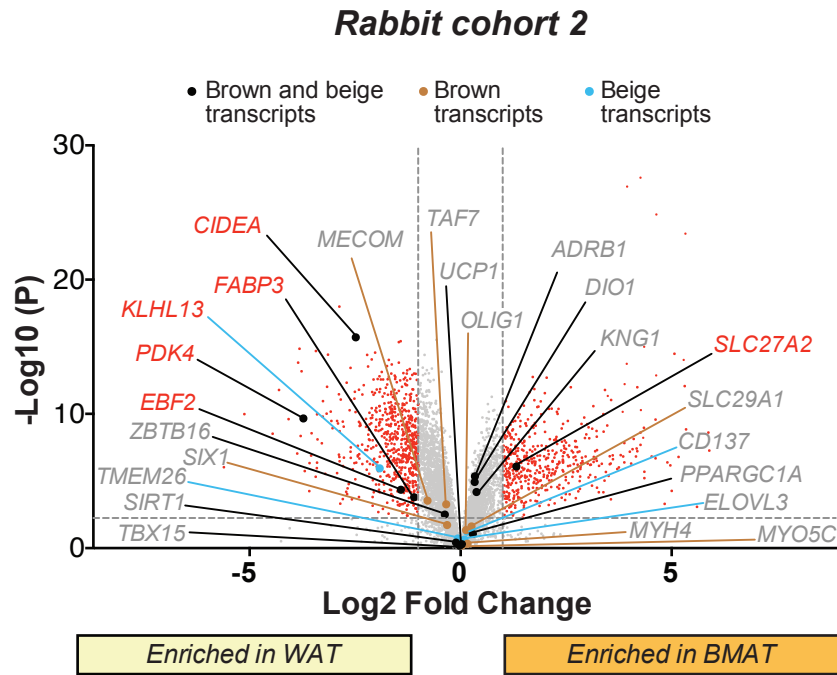


**Figure 4 – Human BMAT is functionally distinct to BAT and is a major site of basal glucose uptake. (A)** Representative MRI (HASTE) and CT images from one subject. **(B)** HU distribution of scWAT, BMAT-rich BM (sternum) and BMAT-deficient BM (vertebrae). Data are mean  $\pm$  SEM (n = 33). Thresholds diagnostic for BMAT (<115) and RM (115-300) are indicated by dashed lines. **(C)** CT images highlighting BMAT or RM identified using the diagnostic thresholds in (B). Tibiae are shown for completeness but were not present in any other available CT scans. **(D,E)** PET/CT analysis of FDG uptake in *No BAT*, *Active BAT* and cold-exposed (*Cold*) subjects. Representative PET/CT scans in (D) highlight the BM cavities of the vertebrae and sternum; arrows indicate FDG uptake in supraclavicular BAT. **(F,G)** FDG uptake in bone tissue, RM and BMAT (F), or BMAT and scWAT (G), of room-temperature subjects (*No Bat* and *Active BAT* groups); Fem. = femur, Hum. = humerus, Clav. = clavicle, Vert. = vertebrae, Stern. = sternum. Data are shown as mean  $\pm$  SEM (E), paired individual values (F) or box-and-whisker plots (G) of 8 (*No BAT*) or 7 (7 *Active BAT*, *Cold*) subjects per group. Significant differences between bone, RM and BMAT are indicated by \* ( $P < 0.05$ ), \*\* ( $P < 0.01$ ) or \*\*\* ( $P < 0.001$ ). Significant differences between *No BAT*, *Active BAT* and *Cold* groups are indicated by # ( $P < 0.05$ ) or ### ( $P < 0.001$ ). See also Figure S4.

# Figure S1

**A**



**B**

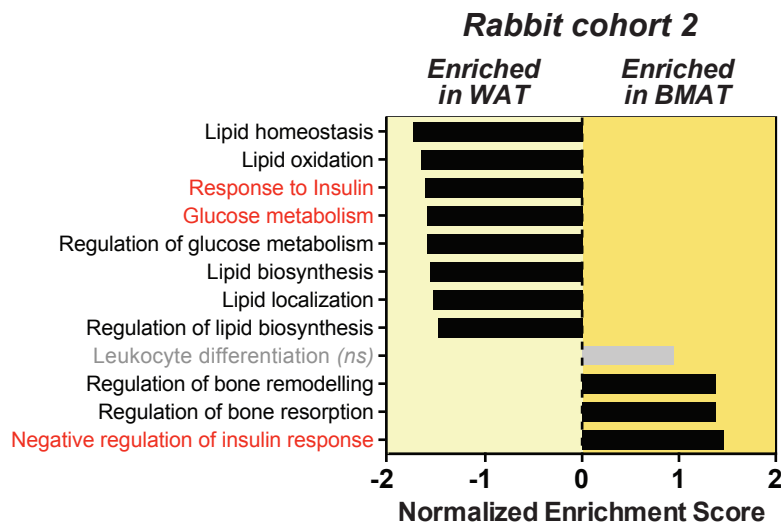
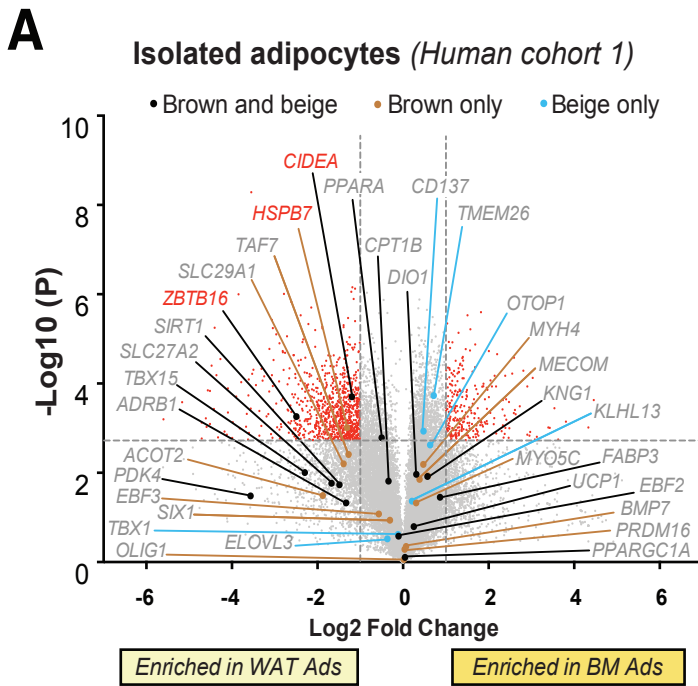


**Figure S1, Related to Figure 1 – BMAT is transcriptionally distinct to white, brown and beige adipose tissues.** Transcriptional profiling of WAT (gonadal + inguinal) vs whole BMAT (dBMAT + ruBMAT) from rabbit cohort 2. **(A)** Volcano plot of differentially expressed transcripts (FDR < 0.05, fold-change > 2). Transcripts characteristic of brown and/or beige adipocytes are labeled. Those with significant differential expression between WAT and BMAT are shown in red; those not differentially expressed are in grey. **(B)** Gene set enrichment analysis (GSEA) highlights lipid metabolism, glucose metabolism and insulin responsiveness as key pathways differentially regulated between WAT and BMAT.

# Figure S2



**B** Isolated adipocytes (Human cohort 1)

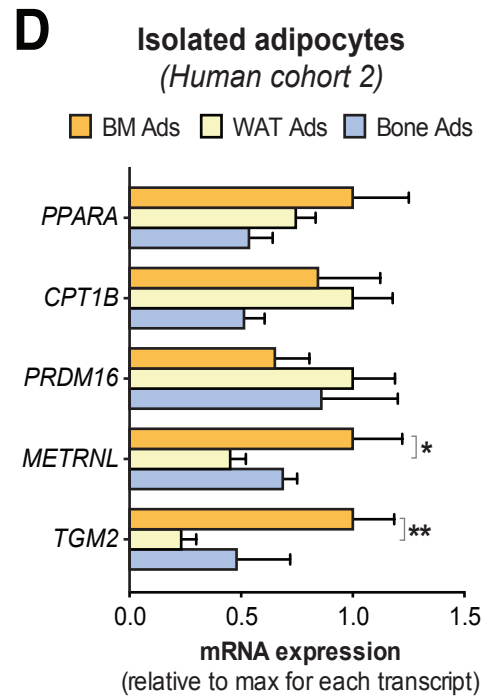
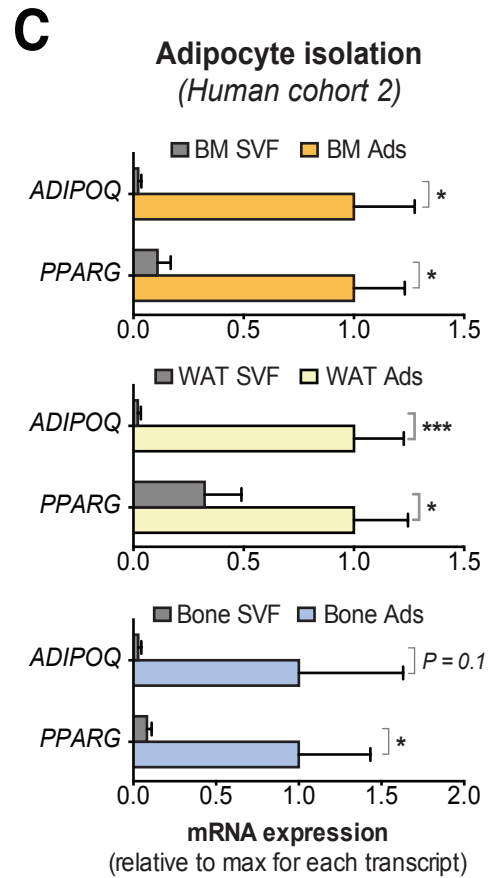
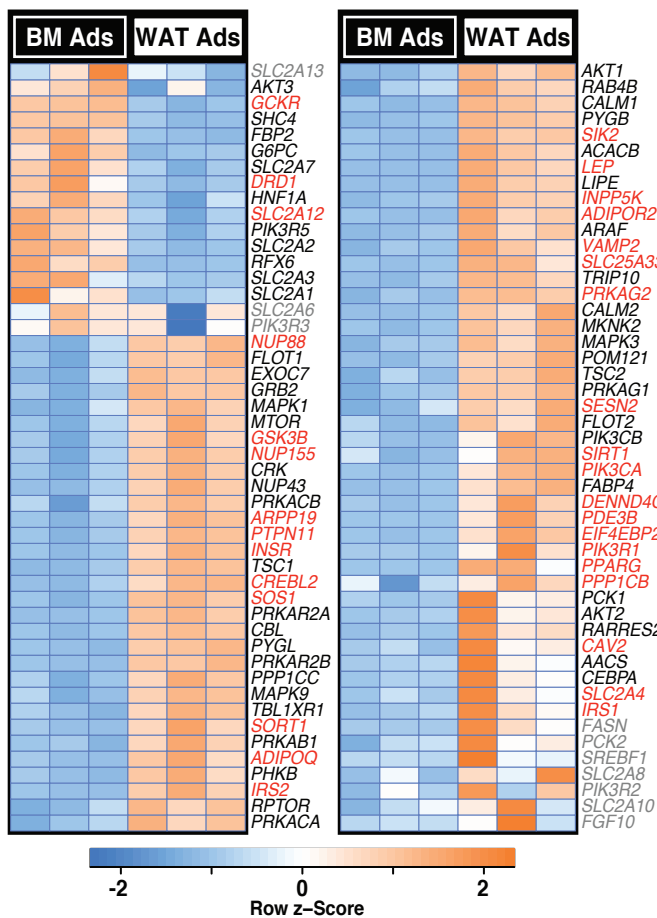
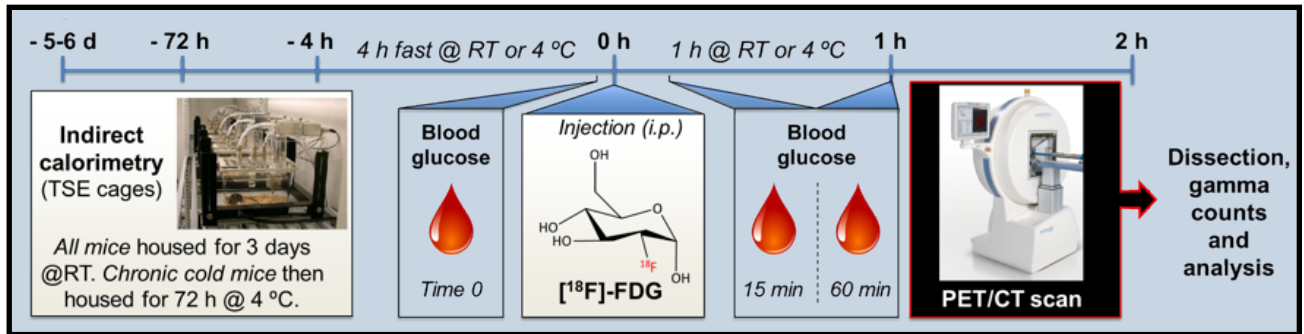


**Figure S2, Related to Figure 1 – BM adipocytes in humans are transcriptionally distinct to those from WAT.** Transcriptional profiling (A,B) and qPCR analysis (C,D) of adipocytes isolated from the subcutaneous WAT or femoral diaphyseal BM of humans undergoing hip-replacement surgery. **(A,B)** Volcano plots (A) and heat maps (B) are presented as for Figures 1 and S1. **(C,D)** qPCR to validate purity of adipocytes isolated from each tissue (C) and showing that BM adipocytes generally do not have increased expression of brown or beige adipocyte markers (D). Transcript expression was normalized to expression of *IPO8* (C) or *RNA18SN5* (D). Data in (C) are mean  $\pm$  SEM of the following numbers per group: BM Ads, n = 8 (*ADIPOQ*) or 9 (*PPARG*); BM SVF, n = 3 (*ADIPOQ*) or 5 (*PPARG*); WAT Ads, n = 10 (*ADIPOQ* and *PPARG*); WAT SVF, n = 5 (*ADIPOQ* and *PPARG*); Bone Ads and SVF, n = 7 (*PPARG*) or 3 (*ADIPOQ*). Data in (D) are mean  $\pm$  SEM of the following numbers per group: BM Ads, n = 3-10; WAT Ads, n = 6-10; Bone Ads, n = 3-7. For each transcript, significant differences are indicated as for Figure 1.

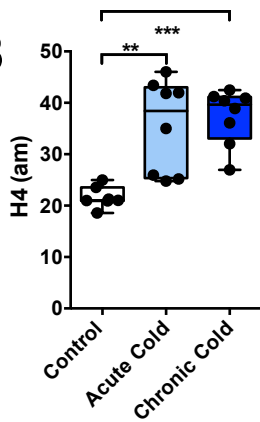


## Figure S3

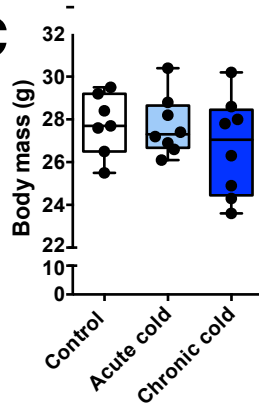
**A**



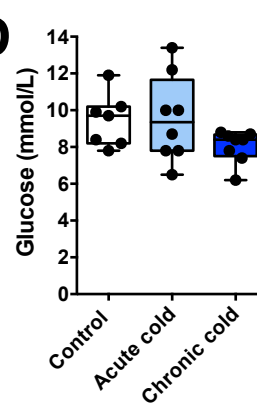
**B**



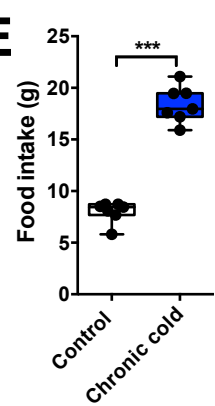
**C**



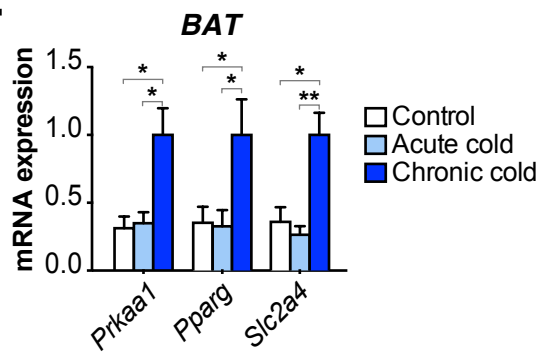
**D**



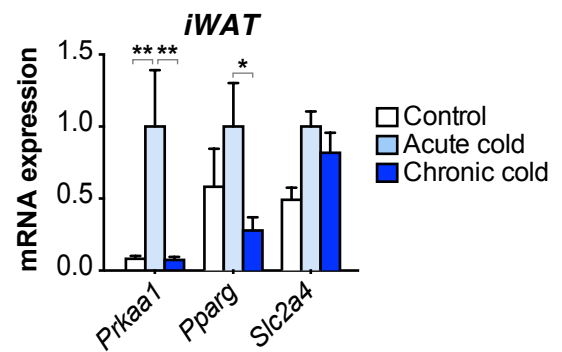
**E**



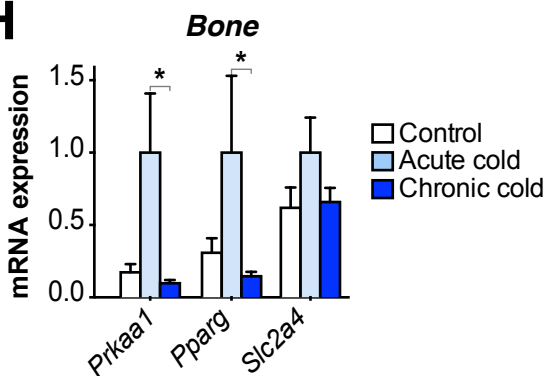
**F**



**G**



**H**



**I**

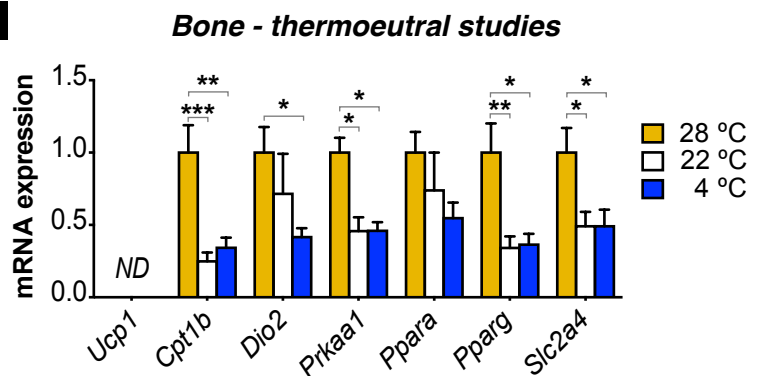


**Figure S3, Related to Figure 3 – Effects of cold exposure on energy homeostasis and gene expression in BAT, iWAT and bone. (A)** Protocol for cold exposure and calorimetry studies, as described in the STAR Methods. **(B-H)** Effects of cold exposure on energy expenditure (B), body mass (C), baseline blood glucose (D), 72 h food intake (E) and transcript expression in BAT, iWAT or whole femurs (F-H). In (E), *Acute cold* mice are not shown because they were fasted throughout cold exposure. **(I)** A separate cohort of mice was housed at thermoneutrality, 22 °C or 4 °C for 48 h. Expression of BAT or beige cold exposure markers was then determined by qPCR of whole femurs. *ND* = not detectable. In (F-I), transcript expression was normalized to expression of *Rn18s* (F,H,I) or *Ppia* (G); the latter was used for iWAT because in this tissue *Rn18s*, but not *Ppia*, showed significant regulation between the three groups. Data are shown as box-and-whisker plots (B-E) or as mean  $\pm$  SEM (F-H) of 7-8 mice per group. In (I), data are mean  $\pm$  SEM of 8-10 mice per group. Significant differences between groups are indicated by \* ( $P < 0.05$ ), \*\* ( $P < 0.01$ ) or \*\*\* ( $P < 0.001$ ).

# Figure S4

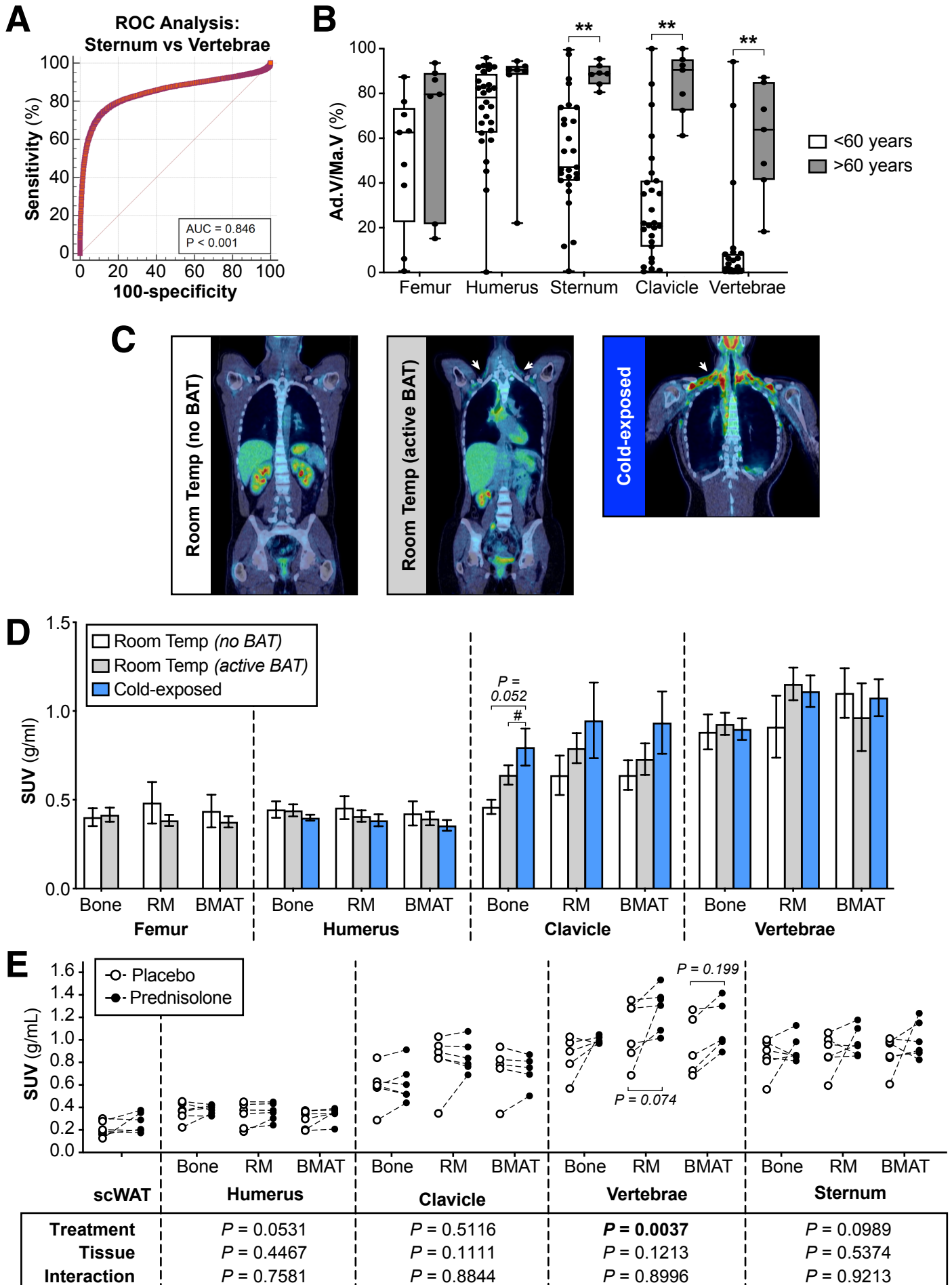


**Figure S4, Related to Figure 4 – PET/CT for identification and functional analysis of BMAT in humans. (A)** ROC analysis to identify HU thresholds to distinguish BMAT-rich (sternum) from BMAT-deficient (vertebrae) regions of BM. **(B)** Quantification of BMAT in CT scans of male and female subjects aged <60 or >60 years. A HU threshold of <115 was used to identify BMAT voxels in BM of the indicated bones, and total BM volume was also determined. The proportion of the BM cavity corresponding to BMAT (Ad.V/Ma.V) was then calculated. Data are shown as box-and-whisker plots of the following numbers of subjects for each group: <60 years, n = 28 (humerus), 9 (femur), or 27 (clavicle, sternum and vertebrae); >60 years, n = 7 for each bone. Significant differences between <60 and >60 groups are indicated by \*\* ( $P < 0.01$ ). **(C)** Representative coronal PET/CT images of *No BAT*, *Active BAT* and *Cold* subjects. FDG uptake in BAT is evident in the *Active BAT* and *Cold* subjects (arrows). Femurs were not included in scans of the *Cold* group. **(D)** FDG uptake in bone tissue, RM and BMAT of the indicated bones. Data are shown as mean  $\pm$  SEM of 8 (*No BAT*) or 7 (7 *Active BAT*, *Cold*) subjects per group. Significant differences between these groups *No BAT*, *Active BAT* and *Cold* groups are indicated by # ( $P < 0.05$ ). **(E)** Subjects were treated with prednisolone or placebo control prior to analysis of FDG uptake by PET/CT. Data are shown as paired individual values for each subject. For each skeletal site, the influence of treatment or tissue (bone, RM, BMAT), and interactions between these, were determined by 2-way ANOVA;  $P$  values are shown beneath the graph.